Surveys in Geophysics (2023) 44:1449–1487
https://doi.org/10.1007/s10712-023-09798-5

Soil Moisture and Sea Surface Salinity Derived from Satellite-Borne Sensors

J. Boutin[1] · S. Yueh[2] · R. Bindlish[3] · S. Chan[2] · D. Entekhabi[4] · Y. Kerr[5] · N. Kolodziejczyk[6] · T. Lee[2] · N. Reul[6] · M. Zribi[5]

Received: 24 August 2022 / Accepted: 22 June 2023 / Published online: 28 August 2023

Abstract
The monitoring of soil moisture and sea surface salinity over the Earth has been profoundly enhanced during the last thirteen years due to a new generation of satellite sensors. L-band radiometry is currently the only technology providing direct measurements of soil moisture, insensitive to surface roughness and distribution of elements in the soil, and the only technology the only technology for measuring that allows us to measure sea surface salinity from space. The Soil Moisture and Ocean Salinity (SMOS) and Soil Moisture Active Passive (SMAP) satellite missions resolve global and local variability with a spatial resolution of approximately 43 km, a swath width close to 1000 km, and a sampling time, for each mission, of at least twice every 3 days. These resolutions and samplings can be increased by either merging data from the two sensors, and with complementary information gathered from other passive or active sensors, or with in situ information at higher spatial resolution. Numerous scientific studies based on the use of this new type of measurement have led to a better understanding and constraint of the processes governing the variability of the water cycle, ocean circulation and the Earth's climate. The continuity of measurements, and the increased spatial and radiometric resolution is critical for fulfilling scientific needs. Future L-band radiometry missions currently being planned in Europe (the Copernicus Imaging Microwave Radiometer), and in China (the Ocean Salinity mission) should provide better constraints on auxiliary parameters by combining multiple frequencies, but they will not have improved spatial resolution beyond SMOS and SMAP. The temporal continuity with SMOS and SMAP will likely not be ensured. In parallel, new concepts are being developed to increase spatial resolution of both land and ocean parameters.

Keywords Soil moisture · Sea surface salinity · Water cycle · Microwave remote sensing

✉ J. Boutin
Jacqueline.Boutin@locean.ipsl.fr

[1] Sorbonne University, LOCEAN/IPSL laboratory, CNRS, IRD, MNHN, 75005 Paris, France

[2] NASA Jet Propulsion Laboratory, California Institute of Technology, Pasadena, CA 91109, USA

[3] NASA Goddard Space Flight Center, Greenbelt, MD 20771, USA

[4] Massachusetts Institute of Technology, Cambridge, MA 02139, USA

[5] CESBIO laboratory, University of Toulouse, CNRS, CNES, IRD, INRA, 31401 Toulouse, France

[6] University of Brest, LOPS laboratory, IUEM, UBO, CNRS, IRD, Ifremer, 29280 Plouzané, France

Article Highlights

- L-band radiometry monitors soil moisture and sea surface salinity from space operationally since 2010
- Satellite soil moisture and salinity reveal variability related to water cycle, biosphere and ocean processes
- Existing scientific studies argue in favor of increasing the spatial resolution of future satellite missions

1 Introduction

Soil moisture (SM) and sea surface salinity (SSS) are key parameters for studying the water cycle, i.e., the exchanges between the Earth's water reservoirs, the ocean, the land, the atmosphere and the cryosphere, as well as for studying the biosphere and the ocean variability. Their measurement from space is particularly relevant as they can be performed at global scale and at spatial resolutions on the order of, or lower than 50 km, while most land and ocean large mesoscale features occur at these resolutions and cannot be observed from in situ measurement networks. The monitoring of SM and SSS has been greatly enhanced since 2010 with the launch of the first L-band radiometer onboard the European Soil Moisture and Ocean Salinity (SMOS) mission, the U.S.-Argentine Aquarius mission (but at a lesser spatial resolution) and the U.S. Soil Moisture Active Passive (SMAP) mission.

This review article aims at reviewing the main advances made possible by passive and active microwave remote sensing of SM and SSS, focusing on spatial resolution of at least 50 km.

In the first part, we detail the main sensors characteristics and the principles for the SM and SSS measurements. Then, we review scientific applications over land and over ocean. In the last part, we present the perspectives for next-generation SM and SSS satellite missions.

2 Spaceborne Sensors and Principle of Measurement for Soil Moisture and Sea Surface Salinity

2.1 Passive Microwave Radiometry

Microwave observations are sensitive to SM and to SSS through the effects of moisture and of salinity on the dielectric constant, and hence, on the reflectivity/emissivity of the soil and of the sea surface, respectively (Ulaby et al. 1986). Vegetation (Jackson and Schmugge 1991) and surface roughness (Choudhury et al. 1979) reduce the sensitivity of the microwave observations to SM. Vegetation and roughness effects become more pronounced as the frequency increases. Hence, low frequencies in the L-band range (~1–2 GHz) are preferred for SM sensing. In this frequency range, radiometry detects emissivity from the top few centimeters of the soil (5 cm on average, see Sect. 3.2.1). The sensitivity of the dielectric constant to the salinity increases as the frequency decreases, and the L-band range is the best compromise in terms of sensitivity, spatial resolution and low disturbances by external effects (atmospheric perturbation, ionospheric Faraday rotation, galactic noise) (Lagerloef

et al. 1995). At L-band, radiometry detects emissivity from the top first centimeter of the ocean (Boutin et al. 2016). Moreover, in order to limit the radio frequency interferences (RFI), the three satellite missions carrying L-band microwave radiometers, SMOS, Aquarius and SMAP, have used the 1.4 GHz protected band (Daganzo-Eusebio et al. 2013).

There are a number of approaches that can be used to retrieve SM from low-frequency passive microwave observations as reviewed in Wigneron et al. (2017). Almost all of these approaches are based on the same radiative transfer equation. This equation requires the estimation of a number of parameters/variables such as physical temperature, vegetation effects, roughness, and soil properties. Over the ocean, only very low-frequency passive measurements are sensitive to SSS. Nevertheless, the sensitivity remains relatively small, and all other contributing effects must be minimized. Therefore, measurement of SSS over the global ocean is currently only feasible using L-band radiometry. SSS is retrieved through full radiative transfer models that involve other variables such as SST and wind speed, and to a lesser extent, atmospheric parameters, as reviewed in Reul et al. (2020).

2.1.1 Soil Moisture and Ocean Salinity (SMOS)

The SMOS mission was launched on 2 November 2009 and is still operating in February 2023 (Kerr et al. 2001). It is an element of the European Space Agency (ESA) Earth Explorer programme and was developed by ESA, the Centre National d'Etudes Spatiales (CNES) and Centro para el Desarrollo Tecnológico Industrial (CDTI) (Kerr et al. 2001). The SMOS mission is covering new grounds in several domains. It is the first L-band radiometer in space achieving a global and continuous coverage. It was also the first satellite to infer SSS and SM directly and in an absolute fashion, i.e., without scaling or change detection with a suitable accuracy (0.04 m^3/m^3 for SM). The instrument concept was also very new as it was the first 2D interferometer in space. This instrument had the advantage of providing fully polarized multi-angular measurements of the surface. It also has an unsurpassed native spatial resolution (~ 30 km at 3 dB below the satellite and 43 km on average over the whole field of view) gridded to 15 km resolution. The price to pay is in terms of sensitivity when compared to traditional radiometers. It is also worth noting that as the scene is reconstructed, the observations are always made at exactly the same point (which can in principle be selected) enabling perfect comparison between different acquisitions and better correction of water land transition. Thanks to the instrument design, the level of the antenna back lobes is very low. However, being the first L-band mission has some drawbacks, e.g., the level of RFI in the protected 1400–1427 MHz band was found to be very high and unexpected (Daganzo-Eusebio et al. 2013).

The mission characteristics are to cover the globe twice in less than 3 days to capture the quickly varying variables, with a dusk/dawn orbit to minimize the humidity and temperature gradients at the land and ocean surface atmosphere interface and minimize Faraday rotation effect thanks to the 06 a.m. orbit.

The calibration relies on the cold and a hot target approach for the zero interferometric baseline receivers which determine the absolute value of the scene brightness temperature (Colliander et al. 2007). Thanks to the three redundant systems (Noise Injection Radiometers), the mission has achieved a very high stability and a very stable calibration (Martín-Neira et al. 2016).

The approach to retrieve the SSS relies on the multi-acquisition process to drastically improve the signal to noise ratio (Boutin et al. 2012; Reul et al. 2012, 2014b). The accuracy of the retrieved SSS strongly depends on the modeling of the physics underlying the

measurement of microwave radiometry, and on the colocation/uncertainty of the needed auxiliary data of sea surface temperature (SST) and wind speed. Thanks to the SMOS measurements, followed by the Aquarius and SMAP measurements, this modeling has been greatly developed (Reul et al. 2020). In particular, parametrizations of the dielectric constant (Boutin et al. 2021b) and of the emissivity of the sea surface due to roughness and foam have been improved and are still the subject of active research (English et al. 2020).

Being a "first" both in terms of instrument and measurements, SMOS had to explore unchartered territories leading to constant and significant improvements in the algorithms. Therefore, the algorithms have evolved considerably and three total reprocessing campaigns have already been carried out. Users should be very wary of using the latest reprocessing version (see a list of various versions on https://www.catds.fr/Products/Available-products-from-CPDC/Correspondance-between-Catds-versions-DPGS-versions), and never combine two versions in any analysis.

Thanks to its characteristics, the SMOS mission has two very important features: (1) it provides the science community with more than 13 years of continuous and homogeneous data and (2) it can be easily and seamlessly merged with other similar missions such as the SMAP mission from NASA.

SMOS delivers a whole range of products. The basic product is Level 1 multi-angular fully polarized brightness temperatures. These temperatures are available in real time, as well as with a slight delay (typically several hours) with an easier format to handle.

Level 2 products are mainly SM, vegetation opacity and SSS. Pseudo-dielectric constant (Waldteufel et al. 2004), RFI maps and other products can also be obtained. SM is also produced in near real time (less than 3 h after acquisition) (Rodríguez-Fernández et al. 2017) and is directly ingested in Numerical Weather Prediction (NWP) models as at the European Centre for Medium range Weather Forecast (ECMWF) (Muñoz-Sabater et al. 2019; Rodríguez-Fernández et al. 2019).

Level 3 SM and SSS global maps are produced operationally at 'Centre Aval de Traitement des Données SMOS' (CATDS). Other Level 3 and Level 4 SM and SSS products are generated in delayed time with refined or alternative algorithms at CATDS, at Barcelona Expert Center (BEC), and in the frame of the ESA Climate Change Initiative (CCI) projects.

Several Level 3 and 4 products are also available either from space agencies or from various institutes, such as Root Zone Soil Moisture (RZSM), disaggregated SM data at 1 km (Molero et al. 2016), water bodies (Parrens et al. 2017, 2019), freeze thaw soil state (Rautiainen et al. 2016), strong winds (Reul et al. 2016), SSS with a spatial resolution increased to 0.05° in global ocean and semi-enclosed basins (Olmedo et al. 2016), SSS corrected from instantaneous rainfall (Supply et al. 2020), sea surface density and spiciness (Kolodziejczyk et al. 2021), thin sea ice thickness (Kaleschke et al. 2016), biomass and carbon (Brandt et al. 2018a; Rodríguez-Fernández et al. 2018; Tian et al. 2018), improved rainfall estimates over land (Pellarin et al. 2020), yield estimates and food security (Gibon et al. 2018), flood risks and fire risks (Chaparro et al. 2016), or drought indices (Ojha et al., 2023).

2.1.2 Aquarius

The Aquarius mission (Lagerloef et al. 2008) was launched on 10 June 2011 onboard the SAC-D spacecraft of the Comisíon National de Actividades Espatiales (CONAE), the Argentinean Space Agency. It carried an L-band radiometer and a scatterometer developed by National Aeronautics and Space Administration (NASA) as the primary sensors. The main scientific objectives were to measure SSS over the global ice-free oceans with a 150-km spatial resolution for a 7-day revisit, and to achieve a measurement error less than 0.2 on a 30-day time scale, taking into account all sensor and geophysical random errors and biases. The Aquarius sensor consisted of horns (3 beams) operating in push broom mode. It viewed continually away from the Sun to avoid signal contamination from solar L-band energy flux. The three beams vary in width and incidence angle to form a 390-km-wide ground swath, with three ground footprints of 74 km × 94 km, 84 km x 120 km and 96 km × 156 km. With an exact repeat cycle of 7 days, Aquarius provides a near global coverage at 7-day intervals. Due to an electronic failure on the SAC-D platform, the Aquarius mission ended on 7 June 2015.

The Aquarius instrument provided much less noisy Level 2 SSS than SMOS due to its better radiometric resolution and because a RFI filtering system was installed onboard based on RFI contamination observed by SMOS (Le Vine et al. 2014). Hence, Aquarius has been considered as a reference for retrieving SSS from L-band radiometric measurements for a long time. However, owing to the frequent revisit of SMOS, and providing that RFI are well filtered out, the precision of monthly SMOS SSS reprocessed with recent algorithms is very close to the one of monthly Aquarius SSS at Level 3 [see Table 4 in Boutin et al. (2021a)]. Moreover, the SSS gradients and eddying features are better detected with SMOS thanks to its better spatial resolution than that of Aquarius (e.g., Hasson et al. 2019; Thouvenin-Masson et al. 2022), and the combination of SMOS and Aquarius SSS enhances the quality of monthly SSS satellite products (Boutin et al. 2021a).

2.1.3 The Soil Moisture Active Passive mission (SMAP)

The SMAP mission (Entekhabi et al. 2010) jointly developed by the Jet Propulsion Laboratory (JPL) and NASA Goddard Space Flight Center (GSFC) was launched on 31 January 2015. The measurement objective of SMAP is to produce global mapping of SM, including its state as frozen or thawed, every two to three days. Originally, SMAP included an L-band radar and an L-band radiometer for coincident active/passive measurements integrated as a single observation system. The radiometer and radar instruments became operational in April 2015. Although the SMAP radiometer has since been operating flawlessly, the radar transmitter ceased operating on 7 July 2015 due to a hardware glitch, leaving the radiometer the only operational instrument collecting science observations (Piepmeier et al. 2017).

Despite this untimely loss, there are several hardware innovations that equip the radiometer with advanced data acquisition capabilities, which were not available in earlier radiometer designs. The 6-m rotating mesh antenna onboard the spacecraft, for example, provides a lightweight yet robust solution to a 360° scanning mechanism that provides not only a wide swath coverage (~ 1000 km) but also full and unobstructed views of fore- and aft-look brightness temperature observations at an effective resolution close to 43 km (Piepmeier et al. 2017). Building on SMOS and Aquarius experiences, the SMAP receivers have the

ability to record time–frequency subband data, which provides an unparalleled flexible way to detect emission contamination caused by manmade sources of RFI that are sparse in time and/or frequency (Mohammed et al. 2016; Piepmeier et al. 2014). This spectrogram-based RFI mitigation approach significantly improves radiometric accuracy and data availability in the presence of correctable RFI. SMAP's successful demonstration of RFI subband data acquisition as well as the use of a large spinning lightweight antenna to achieve a wide swath coverage at fine spatial resolution have influenced the design of several upcoming radar and radiometer missions, including the NASA-ISRO SAR mission (NISAR 2018) and the Copernicus Imaging Microwave Radiometer (CIMR) (Kilic et al. 2018).

The SMAP science data products are provided at various granule extents. Operationally, the Level 1 products include raw/calibrated brightness temperature observations from the radiometer arranged in 6 pm ascending and 6 am descending half-orbit granules. These products include the Level 1B geolocated time-ordered brightness temperatures and the Level 1C brightness temperatures resampled on the Equal-Area Scalable Earth (EASE)-Grid map projections at 9- and 36-km grid resolutions. The Level 2 products, on the other hand, contain SM retrievals derived from the Level 1 products, ancillary data, and other satellite data products. These products include SM estimates retrieved at 9- and 36-km grid resolutions on the same EASE-Grid map projections as the Level 1 products. One particular Level 2 SM product makes use of the Copernicus Sentinel-1 C-band radar observations to achieve global mapping of SM at a 3-km grid resolution with an average revisit interval of up to 12 days. The Level 3 products are in general daily composites of their respective Level 2 half-orbit granules of SM and freeze/thaw state estimates, whereas the Level 4 products include RZSM and carbon net ecosystem exchange generated from state-of-the-art data assimilation models. Near real-time processing streams were also developed to deliver half-orbit granules of brightness temperature and SM products within a few hours of measurement acquisition, supporting a wide range of operational needs ranging from weather forecast, crop growth, to drought monitoring. Ongoing validation activities indicate that all SMAP operational SM products continue to meet or exceed their respective target accuracy, which is 0.04 m^3/m^3 over non-frozen and light-to-moderate vegetated land surfaces (Colliander et al. 2021).

2.1.4 The Advanced Microwave Scanning Radiometer (AMSR)

The AMSR-E of the Earth Observing System (EOS) was developed by the National Space Development Agency of Japan (NASDA) and launched on 4 May 2002 by NASA onboard the Aqua satellite. The AMSR-E instrument measures radiation at six frequencies in the range 6.9–89 GHz, all dual polarized (Table 1). The antenna scans conically at a fixed incidence angle of 55° across a 1445-km swath, providing near-global coverage in two days or less. The spatial resolution at the surface varies from approximately 60 km at 6.9 GHz to 5 km at 89 GHz. The Aqua orbit is Sun-synchronous with equator crossings at 01.30 p.m. and 01.30 a.m. local solar time. AMSR improved upon the capabilities of earlier passive microwave radiometers, such as the Scanning Multichannel Microwave Radiometer (SMMR) and Special Sensor Microwave/Imager (SSM/I).

From 2002 to 2011, AMSR-E onboard NASA's Aqua satellite collected, collecting passive microwave measurements of land and ocean parameters related to global water and energy cycles. As a follow-on instrument to AMSR-E, AMSR2 offers enhanced spatial resolution, better calibration, and improved mitigation of radio-frequency interference. Combining reprocessed AMSR-E data with subsequent AMSR2 observations

Table 1 AMSR frequency channels characteristics

Center frequency	Band width	Polarization	Beam width	Ground resolution	Sampling interval
GHz	MHz		Degree	km	km
6.925/7.3	350	V/H	1.8	35×62	10
10.65	100		1.2	24×42	
18.7	200		0.65	14×22	
23.8	400		0.75	15×26	
36.5	1000		0.35	7×12	
89.0	3000		0.15	3×5	5

provides a nearly continuous record dating back to 2002. AMSR2 has operated since 2012 onboard the Japanese Aerospace Exploration Agency (JAXA) Global Change Observation Mission 1st—Water "SHIZUKU" (GCOM-W1) satellite (http://www.jaxa.jp/projects/sat/gcom_w/index_e.html). Advanced Microwave Scanning Radiometer (AMSR) collection includes passive microwave data products on brightness temperature, precipitation, snow water equivalent, sea ice, SM and sea surface temperature.

Regarding land, measurements at higher frequencies than the L-band range, in the C- and X-band ranges (~6.8–10 GHz), have been shown to be sensitive to SM, but primarily in regions of low vegetation (Jackson et al. 2002; Wigneron et al. 1995). The increased attenuation by vegetation and the shallow sensing depth (on the order of 1 cm for bare soil) at C-band impose limitations on the retrieval of SM by AMSR. Implementing theory into a practical SM retrieval algorithm requires a reduction in the dimensionality by making simplifying assumptions or by providing a priori estimates of some parameters (ancillary data). If all of these factors are considered to be significant and are incorporated into the algorithm, this can result in an under-determined system of equations (i.e., more unknowns than measurements), regardless of how many frequencies and polarizations are available.

The AMSR2 data record is further planned to be extended with the planned launch of the AMSR3 instrument in 2024, potentially leading to a consistent long-term climate data record obtained from the same instrument. The availability of such a long-term global data record will benefit research studies that require information on long-term SM trends. AMSR provides important long-term information over large areas of the globe, particularly in the dynamic transition zones between arid and forested areas where the SM is most variable and unpredictable.

In addition, the potential SSS retrieval capability from the differential sea surface vertically polarized emissivity contrast between the C-(6.9 GHz) and X-(10.7 GHz) bands AMSR-E data has been demonstrated in Reul et al. (2009) for the very high SSS gradients and the warm Amazon river Plume areas. While the frequency differential contrast is significantly less sensitive to SSS than in the L-band (1.4 GHz), it minimizes the impact of sea surface temperature and wind speed, allowing the strong SSS signals to be monitored. This principle was recently applied to the SSS signal in the China Sea using the same frequency channels data from the microwave radiometer onboard the Chinese HY-2A satellite (Song and Wang 2017). As currently developed in the ESA Climate Change Initiative (Boutin et al. 2021a), the common operation period between AMSR-E and SMOS (January 2010–October 2011) can be exploited to best tune the AMSR-E SSS retrieval algorithm.

Combined with the dedicated L-band sensor era (2010-now), this shall allow the generation of the longest satellite-based climate SSS time series in some warm tropical large river plume regions, e.g., Amazon and Orinoco, Mississippi, Congo and Niger, Bay of Bengal.

2.2 Active Remote Sensing of Soil Moisture

Active techniques are complementary to passive microwave radiometry. In contrast to radiometry, active techniques are much affected by structure parameters of the vegetation and surface roughness, at first order. On the other hand, they provide a better spatial resolution on the order of one kilometer.

2.2.1 Reflectometry

Satellite reflectometry offers a new data source for remote sensing of SM. Reflectometer is a bistatic radar with the transmitter and the receiver separated from each other. The transmitted signal is bounced off the earth surfaces into the receiver with the dominant contribution expected to be around the specular point.

L-band Global Navigation Satellite System (GNSS) signals were well matched for reflectometry due to their use of pseudo-random noise (PRN) codes for ranging. The GNSS-based Reflectometry (GNSS-R) was initially developed for ocean altimetry (Hajj and Zuffada 2003; Martin-Neira 1993) and has been extended to land remote sensing. The significant advancements in GNSS-R technologies in the past two decades led to the selection of the Cyclone Global Navigation Satellite System (CYGNSS) mission by NASA (Ruf 2012). It has been launched on 15 December 2016. CYGNSS observatories make single circularly polarized reflectivity observations at the Global Positioning System (GPS) frequencies (1.5 GHz).

The theoretical principle of inferring SM from GNSS-R data is based on the response of L-band microwave reflectivity to SM (Zavorotny et al. 2010). Several empirical approaches for SM retrieval from CYGNSS data have been published based on the collocations of CYGNSS data and SMAP SM by using linear regression (Chew and Small 2018; Clarizia et al. 2019; Kim and Lakshmi 2018) and artificial neural network trained with the in situ station data (Eroglu et al. 2019). These empirical approaches can produce reasonable performance for SM retrieval over regions with a sufficient correlation between CYGNSS data and SMAP SM. However, over most parts of the CYGNSS coverage, the empirical correlation was low (<0.3), leading to a poor performance for CYGNSS SM retrieval (Chew and Small 2018).

Alternatively, the change of SM over semi-arid regions and many agriculture regions from CYGNSS can be improved using a semi-empirical model based on the dielectric constant model of soil used by the SMAP and SMOS missions. It relates the CYGNSS reflectivity to SM, vegetation water content, and rough surface scattering (Yueh et al. 2020b).

An alternate approach to independent SM retrieval for each acquisition time is to focus on the SM changes in the time series of CYGNSS observations (Al-Khaldi et al. 2019). This time series approach can avoid the drawback of empirical regression algorithms, but requires a high-quality SM product, such as that from SMAP, for scaling the CYGNSS data into SM.

2.2.2 Synthetic Aperture Radar

Over the past thirty years, Synthetic Aperture Radar (SAR) remote sensing has shown great potential in estimating SM at the agricultural plot scale, which is essential for water resource management.

In the case of bare soils, the SAR radar signal, which is affected by three different radar parameters (polarization, incidence angle and frequency), is also correlated with soil surface roughness and moisture content (Baghdadi and Zribi 2016; Ogilvy and Merklinger 1991; Ulaby et al. 1978, 1986). In recent decades, various algorithms have been proposed to retrieve SM using machine learning (El Hajj et al. 2017; Ezzahar et al. 2020; Notarnicola et al. 2008; Paloscia et al. 2013; Santi et al. 2016), change detection techniques (Bauer-Marschallinger et al. 2018; Foucras et al. 2020; Gao et al. 2017), direct inversion of a scattering model of a single radar signal, or more radar configurations [e.g., multi-incidence (Zribi and Dechambre 2003), multipolarization (Wang et al. 2019), multifrequency (Bindlish and Barros 2000)].

These different approaches have been enhanced with the Copernicus Sentinel-1 mission launched on 3 April 2014, which has allowed strong temporal repetitiveness adapted to the needs of water resource use at the local scale. A synergy with Sentinel-2 optical data through indices such as Normalized Difference Vegetation Index (NDVI) is much used to parameterize the effect of vegetation in the radar signal backscattered by the land surface. The proposed approaches allow access to agricultural plots (El Hajj et al. 2017) or an intermediate scale of approximately 1 km (Bauer-Marschallinger et al. 2018; Foucras et al. 2020). For the latter, numerous disaggregation and synergy approaches have been developed between radar data and low-resolution active or passive microwave data (Amazirh et al. 2019; Kim et al. 2017b). In this context, various operational SM products have been developed at intermediate resolutions (1 km, 3 km, etc.), particularly based on the synergy between SMAP and Sentinel-1 data (Das et al. 2019).

3 Soil Moisture Science and Applications

3.1 Science Results from SMOS

SMOS has been in operation for more than 13 years and still operates flawlessly. Throughout these years, several steps had to be carried out to ensure scientific successes, as it was both the first L-band mission and the first interferometer in space. The focus was first put on basic variables (SM and SSS), but several other science domains and applications very quickly emerged. This very rapid transition is due to the fact that for the first time a space instrument (L-band radiometer) could give direct access and in an absolute fashion to SM (i.e., without scaling, change detection or strong assumptions).

3.1.1 Soil Moisture and Derived Quantities

SMOS SM and vegetation opacity (VOD for Vegetation Optical Depth) are retrieved directly from the SMOS multi angular measurements. The retrieval scheme is based on a minimization of a cost function (Kerr et al. 2010) and has no empirical or change

detection caveats. The products are available globally from deserts to tropical rain forest with an accuracy only related to the vegetation density (Kerr et al. 2016). Data resolution is typically 40 km and they are delivered on a 15 km grid.

The first direct application was to infer RZSM from SM using simplified approaches (Ford et al. 2014). This led to a number of very interesting research topics such as the elaboration of reliable drought indices and the analysis of interactions between water storage and vegetation stress. SM also proved to be a very important variable when assessing flood risks (Baugh et al. 2020; Mecklenburg et al. 2016). With soil saturation coupled with heavy rainfall forecasts, it is possible to delineate area where flood risks (or flash floods in another context) are very likely (Laachrate et al. 2019). A feasibility study showed that the main limitation to set up such a flood forecast system was the accuracy of the precipitations (Mecklenburg et al. 2016). The SM obtained by SMOS is also useful for sand dust prediction (Gherboudj et al. 2015; Kim et al. 2017a). One limitation of SM products is their current spatial resolution. Many efforts have been made to infer higher resolution products for use in agriculture and hydrology (Verhoest et al. 2015). High-resolution SM fields were derived using different disaggregation approaches relying either on optical data sets (Molero et al. 2016) or on radar/SAR measurements (Tomer et al. 2016). They enabled studies on, e.g., irrigation (Dari et al. 2021; Paciolla et al. 2020), desert locust early warning (Escorihuela et al. 2018). Such approaches have also been used to get finer information on other variables such as biomass and water bodies (see below). It is well understood that the quality of the outputs is slightly degraded when compared to the quality that would be obtained by a real radiometer with a higher resolution, but it fills a gap.

Having access to either brightness temperatures or SM fields in near real time fostered the use of SMOS in NWP models (Rodríguez-Fernández et al. 2017). At ECMWF, near real-time data were used first for monitoring and then, assimilated in the model. The results show limited improvements because model assimilation schemes were not designed to assimilate absolute measurements of SM (Muñoz-Sabater et al. 2019). In summary, SMOS SM was improved relative to other techniques providing indirect SM estimates, without necessarily improving the assimilation scores. SMOS significantly contributed to establishing where NWP models have issues and need improvements to be able to assimilate not only SMOS but also other sensors in land data assimilation systems (Crow et al. 2020).

The precipitations derived from satellite are very useful, but they suffer from inaccuracies in several areas (see a review in Pellarin et al. 2020). Using an assimilation scheme ingesting SMOS data enabled to significantly improve rainfall estimates (Pellarin et al. 2020; Roman-Cascon et al. 2017). Using such information was also very useful for food security programs as demonstrated as early as 2011 by W. Crow at United States Department of Agriculture and then by Gibon et al. (2018).

SMOS data proved to be also useful in hydrology. First studies were made to see how assimilating SMOS data in hydrological models could improve model outputs (Lievens et al. 2015), and recent studies showed that some improvements were noticeable (Fleischmann et al. 2021). Other groups studied the monitoring of water bodies below dense canopies with a relatively high temporal sampling, quantities that are not necessarily measurable from space with other sensors (Parrens et al. 2017, 2019). This led, e.g., to a seasonal monitoring of the Amazon and Congo basins, and this monitoring could be improved using disaggregation approaches (Parrens et al. 2019). This offered the first opportunity to understand and monitor the hydrology of these large basins largely covered with dense forests. With now more than 13 years of data including several El Niño/La Niña events, we can better describe and thus, understand climate teleconnections. Monitoring water bodies

also opens a new research field related to gas exchanges between water bodies and the atmosphere.

3.1.2 Vegetation Opacity

SM and vegetation opacity (also called VOD) can both be inferred using the multi-angular capability of SMOS (Kerr et al. 2001, 2016; Wigneron et al. 2000). VOD is part of the SMOS data since the beginning of the mission, but it suffered in the early stages from the trial and errors of accurate image reconstruction and associated calibration. After the second SMOS mission reprocessing though, brightness temperatures became sufficiently reliable to be used even over dense canopies to infer VOD, which is linked to low vegetation water content (i.e., grass, crops, etc.) and branch/ trunk biomass for trees and forested areas. The relationship between VOD and tree height (and thus biomass) was shown at an early stage in the SMOS mission to be clear (Rahmoune et al. 2014), but since the last reprocessing, significant advances were made leading to a number of very significant results related to biomass monitoring (Brandt et al. 2018a, b; Fan et al. 2018; Tian et al. 2018) and more generally to carbon related issues (Scholze et al. 2019).

Monitoring both biomass and vegetation water content together with SM obviously puts forward a new venue in terms of deforestation and deforestation-related impact, fire risks mapping or fire recovery. For instance, intense deforestation could be readily associated with a decrease in SM and a large increase in the seasonal cycle of SM (Bousquet et al. 2022).

3.1.3 Cryosphere

SMOS also proved to be a very valuable tool to monitor cryosphere even though this was not a priority at launch. The first application was to infer thin sea ice thickness as the signal is very complementary to that of altimeters such as CryoSat-2. SMOS measures thin sea ice well, while CryoSat measures well thick sea ice (Kaleschke et al. 2016, Tian-Kunze et al. 2014). By combining both measurements, sea ice can be monitored globally with an unprecedented accuracy in the Artic polar cap which shrinking trend since 2010 can be described, and sea ice around Antarctica can also be monitored.

Studying Antarctica also enabled to make significant progresses in terms of assessing snow melt periods (which are increasing regularly), and ice sheet internal temperatures (Leduc-Leballeur et al. 2020). SMOS also allows assessing the amount of water in liquid form in either snow or ice, opening new paths on Greenland deep melting and avalanche risks mapping (Houtz et al. 2021; Naderpour et al. 2021). Such results are leading to the possibility in the mid-term to reach at long last a way to estimate snow water equivalent (Houtz et al. 2019).

Over land masses, a freeze thaw (F/T) detection approach was established soon after the launch of SMOS at the Finnish Meteorological Institute due to the sharp change in dielectric constant when soil freezes, giving way to an operational F/T product (Rautiainen et al. 2014, 2016). This information is obviously of paramount interest for assessing climate-induced changes at high latitudes, but it can also be related to methane exchanges that are very much related to the thawed period. To improve this high latitude monitoring further, as L-band enables to estimate soil's temperature below a snow layer, studies to monitor soil temperature throughout the year and thus to monitor permafrost extent variations have been initiated, capitalizing on the more than 13 years of SMOS data.

Finally, it was recently found both theoretically, and at ground and satellite levels, that the dielectric constant (hence, VOD) of vegetation undergoes huge changes around 0 °C at L-band, meaning that, if not done carefully, estimates of biomass at high latitudes could be erroneous (Schwank et al. 2021).

3.1.4 Summary

After 13 years in space, and being the first of its kind, SMOS has enabled a wealth of science results which cannot be summarized in a few pages. The results also cover a very large range of science topics going from smart irrigation to climate trends, and from desert locust warning to dust transport. The impressive publication record is one of the most traceable indicators of success, and should the satellite continue to operate nominally for several years, new insights of our changing climate will become available.

3.2 Science Results from SMAP

Given the central role of SM and its freeze/thaw state in the Earth system, SMAP's frequent global mapping addresses a wide range of Earth system science and applications objectives (Entekhabi et al. 2014). We review below the main results obtained for each SMAP overarching scientific mission goal.

3.2.1 To Estimate Global Surface Water and Energy Fluxes

The first science goal of the SMAP project was to estimate global water and energy fluxes at the land surface. These fluxes are key determinants of the global water, energy and biogeochemical cycles. Direct and in situ measurements of these fluxes are limited to several hundred point-locations using eddy-covariance instruments. Their underlying processes are parameterized in Earth System models and the variations in the approach to their parameterizations result in large deviations among models on how they characterize the dynamics of the global water, energy and biogeochemical cycles.

The influence of SM availability on water, energy and biogeochemical fluxes at the land–atmosphere interface extends beyond surface SM and involves the profile of SM at least down to the extent of vegetation roots. L-band frequency radiometry detects emissivity from the top few centimeters of the soil (about 2–20 cm depending on the SM). SMAP science data products provide an estimate of the top 5 cm on average. However, the sensing depth should not be confused with SM information inherent in the measurements. The SM profile is continuous, and the dynamics of an extended profile is evident in the surface measurements. To specifically address this topic, Akbar et al. (2018) and Gianotti et al. (2019b) address the question of the effective depth of the SM profile represented in the dynamics of SMAP measurements. Using two independent approaches, they both find that the dynamics in the measurements represent the dynamics of the SM profile that can extend to about 50 cm depending on soils, vegetation and climate, but the median is about 15 cm. The estimates and methodologies are verified using in situ stations where the SM profile is measured at multiple depths below the surface.

3.2.2 To Quantify Net Carbon Flux in Boreal Landscapes

The second SMAP science goal was to understand processes that link the terrestrial water, energy, and carbon cycles, which can be considered among the primary metabolic cycles of the Earth system (Buontempo 2022). The cycles are connected, and, as a result, perturbations in one cycle can affect the other cycles. How strongly or weakly they are connected determines the propagation of perturbations across the cycles. Earth System models inherently include these connections. The linkages are formed through parameterizations that vary greatly among the models. As a result, a major contributor to the uncertainty in climate projections can be traced to how they couple these cycles. Over land, the coupling between the water and energy cycles can be captured through a diagnostic that is the plot of Evaporative Fraction (EF) versus SM. The EF-SM relation should capture the transition between water-limited and energy-limited evapotranspiration regimes. The diagnostic succinctly captures many detailed processes coded within models.

Gianotti et al. (2019a) diagnosed the linkage between the water and energy cycles in six CMIP5 Earth System Models. There is a wide range of coupling strengths among the models resulting in varying responses of the water and energy cycle to perturbations. The discordance is troubling. Gianotti et al. (2019a) use SMAP SM and evapotranspiration estimated using the weather station network across the continental USA to perform the same diagnostic but based on observations alone. The authors showed evidence of a systematic transition from water-limited to energy-limited evaporation regimes with increasing available SM. The plateau for the energy-limited regime depends on the dominant biome and climate. In the water-limited regime where EF is reduced with reduced SM, the slope of the EF-SM function is the strength (degree) of coupling between the water and the energy cycles. The authors produced the same results for the coupling between the water and the carbon cycles. They use Solar-Induced Fluorescence (SiF) from satellite measurements that are indicative of the amount of Gross Primary Productivity without use of models. In this case, the diagnostic is landscape Water Use Efficiency (WUE), which is the ratio of carbon-to-water exchange at the land surface.

3.2.3 To Reduce Uncertainty of Climate Model Projections

The third SMAP science goal was to quantify net carbon flux in boreal landscapes. Amplified winter warming in the Arctic is expected to cause large-scale shifts in the biogeochemical cycles in the region. Changes in the seasonal patterns of inundation, permafrost, landscape freeze/thaw and SM are the primary drivers of the biogeochemical flux shifts. SMAP measurements are used to map and quantify these variables. This unique capability of SMAP motivated the development of SMAP Level-4 products that assimilate radiometric SMAP observations in conjunction with other satellite measurements, in situ observations, and models in order to produce a comprehensive picture of water and carbon processes—including frozen and thawed seasons—across the boreal latitudes.

The SMAP Level-4 Carbon (L4C) products have been used in many studies. Natali et al. (2019) studied enhancements in soil CO_2 emissions due to interannual climate variability in the boreal latitudes, which show Boreal-Arctic seasonal CO_2 uptake. There are large differences among the models when compared with the SMAP L4C and estimates based on flux towers. This highlights the remaining uncertainty on the understanding of the climate-biogeochemical linkages that form the basis for the construction of these models. SMAP

mapping of the key drivers of the climate-biogeochemical linkages and flux tower data taken together are actively used to test and further develop these models.

Liu et al. (2020) examined the net landscape carbon exchange with the atmosphere due to changes in the date of freeze in Autumn and in the date of thaw in Spring. Landscape freeze/thaw is conceptually the on/off switch for processes that constitute the components of this carbon budget. Boreal-Arctic ecosystems strongly impact the larger global carbon budget and can be either a net annual sink or source for atmospheric CO_2. Using SMAP freeze/thaw and L4C products, Liu et al. (2020) found that landscape photosynthetic carbon-gain in warmer springs is offset by winter respiration carbon losses resulting in near-neutral annual C-balance. Net Ecosystem Productivity (NEP) is calculated as the difference between gross primary production (GPP) and terrestrial ecosystem respiration. In terms of process-understanding, they find that temperature is the dominant control on carbon exchange in Spring and Winter, while SM is dominant in Autumn, with greater moisture limitations in boreal forests than tundra.

3.2.4 To Improve Flood Prediction and Drought Monitoring

The fourth SMAP science goal was to develop improved flood prediction and drought monitoring capability. Sadri et al. (2018) assessed SMAP SM in terms of probability percentiles for dry and wet conditions. They compared the SMAP-based drought index maps with metrics such as the operational US Drought Monitor (Svoboda 2000), 1-month Standard Precipitation Index (SPI; https://climatedataguide.ucar.edu/climate-data/standardized-precipitation-index-spi) and a hydrologic model output for estimated SM. This study is a step forward toward building an international SM monitoring system. Sadri et al. (2018) also used SMAP data to identify regions of anomalously wet conditions that can be valuable for water management purposes. The SMAP-based drought index shows greater consistency with the operational US Drought Monitor when compared to SPI and the integration of the Variable Infiltration Capacity (VIC, as referred to in Sadri et al. (2018)) land surface model. Togliatti et al. (2019) proposed a forward-looking approach to monitoring crop water stress, which is one of the more important impacts of drought. They used SMAP measurements to directly estimate VOD, the degree to which vegetation attenuates microwave radiation. VOD is retrieved along-side SM and is related to the total amount of liquid water in a vegetation canopy. Thus, VOD allows direct monitoring of seasonal changes in crop water that allows predictions of yield or crop failure. A main advantage of SMAP VOD over optical/infrared indices is that clouds do not lead to data gaps at critical and rapid growth stages of crops.

In the area of flood monitoring and forecasting, a forward-looking example of developing next-generation and modernized approaches is the introduction of surface inundation fraction using the SMAP radiometer. The accuracy and reliability of flood assessments are dependent on the availability of continuous and high-quality precipitation information. Such continuity and quality are often not available in real-time especially in developing countries where the hazard impacts are amplified. Optical monitoring of flood extent is often limited by cloud cover. Wu et al. (2019) investigated the global consistency of surface fractional water inundation retrievals from SMAP versus modeled runoff from the University of Maryland Global Flood Monitoring System (GFMS). Wu et al. (2019) showed that favorable SMAP-GFMS correspondence ($r \geq 0.4$) is evident over a majority (64%) of the global domain; stronger correlations occur in drier climates with low to moderate vegetation cover and large seasonal flood range. Synchronous flood dynamics appear over 33%

of the global domain, but SMAP inundation fraction and GFMS flooding in other areas also appear to have a lag of up to three months. SMAP and GFMS provide complementary information on water storage changes affecting precipitation-driven runoff and flooding, which may enable enhanced global flood predictions.

3.2.5 To Enhance Weather Forecasts

The fifth science goal of SMAP was to enhance weather and climate forecast skill. Much of the solar energy that contributes to weather and climate dynamics is ultimately made available to the atmosphere via surface heating. Over land surfaces, the available energy is dissipated by turbulent fluxes (sensible and latent heat) and thermal radiation. The partitioning among sensible and latent heat fluxes is a key determinant of the heating and moistening of the atmospheric boundary layer which in turn drives thermally driven air motion and moist processes. The skill of NWP models depends on the accuracy of their initial conditions as atmospheric dynamics as a chaotic system is highly sensitive to initial conditions.

For this SMAP science goal, Dong and Crow (2018) analyzed the pathways and patterns of SM influence on the atmospheric boundary layer. They quantified the coupling strength between the land surface boundary condition and the lower atmosphere over the European continent, to build on prior benchmark studies on the 2003 European heat wave and drought resulting in tens of thousands of deaths (Robine et al. 2008). Comparisons with Soil Moisture-Air Temperature-based estimates suggest that the Soil Moisture-Air Temperature Coupling (SMTC) strength provided by seven Coupled Model Intercomparison Project Phase 5 (CMIP5) General Circulation Models (GCMs) generally underestimate SMTC strengths—particularly in central Europe. This result is consistent with previous modeling work and highlights the value of L-band soil moisture remote sensing for land surface-atmosphere coupling analyses.

In another study to highlight the role and impacts of SM on the lower atmosphere, Feldman et al. (2019) used two observational sources to diagnose the pathways that are independent of models and can therefore serve as benchmarks for performance and guide model developments. The SMAP SM product was used in conjunction with the geostationary European Organisation for the Exploitation of Meteorological Satellites (EUMETSAT) Meteosat Second Generation (MSG-2) satellite. The thermal infrared measurements from the MSG-2 Spinning Enhanced Visible and InfraRed Imager (SEVIRI) instrument allow estimation of the diurnal amplitude of the land surface temperature. The MSG-2 geostationary disk covers Africa and Europe. The nadir for the satellite instrument is the Equator over Africa, and hence, highest quality data are available over this continent. Feldman et al. (2019) isolated dry-downs (inter-storm periods) within SMAP data over Africa spanning diverse biomes and climates for analysis. SM is monotonically decreasing during dry-downs, and the evaporative fraction functional form with SM is being traversed from energy-limited regime at the beginning of the inter-storm period (wetted soils) to water-limited regime as the soil continues to dry. The threshold signifying the transition between the regimes has consequences for the land surface temperature state and its diurnal amplitude. Once in the water-limited regime, the more efficient turbulent flux cooling mechanism or latent heat flux is diminished in favor of more partitioning toward sensible heat flux. This is evident in the increase in observed diurnal temperature range across biomes, especially transitional sub-humid zones. The threshold behavior is evident in the shape of the curves which begin in time-into-dry-down as flat (energy-limited regime) to rapid warming during the water-limited regime. The lower atmosphere is impacted by this

warming response. Due to reduced evaporation rates, the reduced latent heat flux cooling goes hand-in-hand with reduced moisture flux. The boundary layer response is reduced humidity. Increased warming at the base of the atmosphere results in more growth in the atmospheric mixed-layer and entrainment of dry air from above which further reduces the humidity in the lower atmosphere.

4 Sea Surface Salinity (SSS) Science and Applications

Ocean surface water masses are primarily defined by the SST and the SSS, building the Sea Surface Density (SSD), and featuring the ocean with fronts and jets, eddies and filaments. These oceanic features control the thermohaline circulation, ocean meso-scale and submeso-scale instabilities. They have a subsequent impact on water mass transformation, subduction and mixing, and can impact the ocean–atmosphere interaction. Some contributions of satellite SSS to improving the understanding of large-scale SSS variations and their relationships with ocean circulation and climate variability, of the water cycle (river plumes) and of frontal dynamics are highlighted below. There have also been a vast body of literature documenting contributions of satellite SSS to the studies of oceanic variability and circulation in open ocean, coastal oceans, and marginal seas, some of which also involve ocean–atmosphere interactions (cf. review articles by Vinogradova et al. (2019) and Reul et al. (2020)). Some of the most striking features are described below.

4.1 Large-Scale SSS Variations and Relations with Ocean Circulation and Climate Variability

With their near-uniform spatiotemporal sampling, satellites have enhanced the capability to characterize the variations of large-scale SSS patterns in the world ocean (Boutin et al. 2021a) and shed light on the roles of atmospheric forcing, ocean circulation, and potential feedback to the atmosphere. These measurements have also elucidated the linkages of large-scale SSS patterns with various modes of climate variability such as El Niño-Southern Oscillation (ENSO), Indian Ocean Dipole (IOD), monsoon, and Madden–Julian Oscillation (MJO).

ENSO, a dominant mode of interannual climate variability due to ocean–atmosphere interaction in the tropical Pacific sector, has far-reaching influence around the globe with important societal impacts including those on weather and precipitation patterns, agriculture, marine ecosystems, and human health (e.g., McPhaden et al. 2006, 2020b). Satellite data have enabled detailed characterizations of large-scale SSS variations and sharp SSS fronts associated with ENSO in different parts of the tropical to subtropical Pacific Ocean (e.g., Guimbard et al. 2017; Hasson et al. 2014, 2018; McPhaden et al. 2020a; Qu and Yu 2014). In the equatorial Pacific Ocean, zonal translations of the eastern edge of the Western-Pacific (WP) Warm Pool edge (29 °C isotherm) and WP Fresh Pool (34.8 pss isohaline) are pivotal to ENSO development because of their effects on air-sea interaction. Satellite-derived SSS and SST show that the movement of the WP Fresh Pool is coherent with ENSO indices (e.g., Nino3.4 SST and Southern Oscillation index) due to combined effects of local precipitation anomaly and advection by anomalous zonal currents associated with ENSO (Hasson et al. 2018; McPhaden et al. 2020a; Qu and Yu 2014). Its movement is also consistent with that of the WP Warm Pool edge, reflecting the potential role of near-surface salinity on upper-ocean mixing of heat and thus, on SST and subsequent air-sea interaction.

The seminal study of the extreme El Niño event in 1997–1998 by Picaut et al. (2002) provided an iconic description of the evolution of that event using multi-variate satellite measurements of SST, Sea Surface Height (SSH), and ocean surface winds. The advent of salinity remote sensing now allows us to provide a more comprehensive, multi-variate characterization of ENSO evolution by including satellite-derived SSS as well (Fig. 1). During the peak of the last extreme El Niño event in 2015, negative SSS anomaly with a magnitude over 1 pss was found in the central-equatorial Pacific between 160°E and 160°W and between the equator and 2°S with a sharp gradient near the equator (Fig. 1c). The center of the precipitation anomaly, however, was located between the dateline and 140°W and skewed north of the equator (0°–5°N) (Fig. 1b). The mismatch of SSS and precipitation anomalies reflects the importance of anomalous ocean currents (also shown in Fig. 1b).

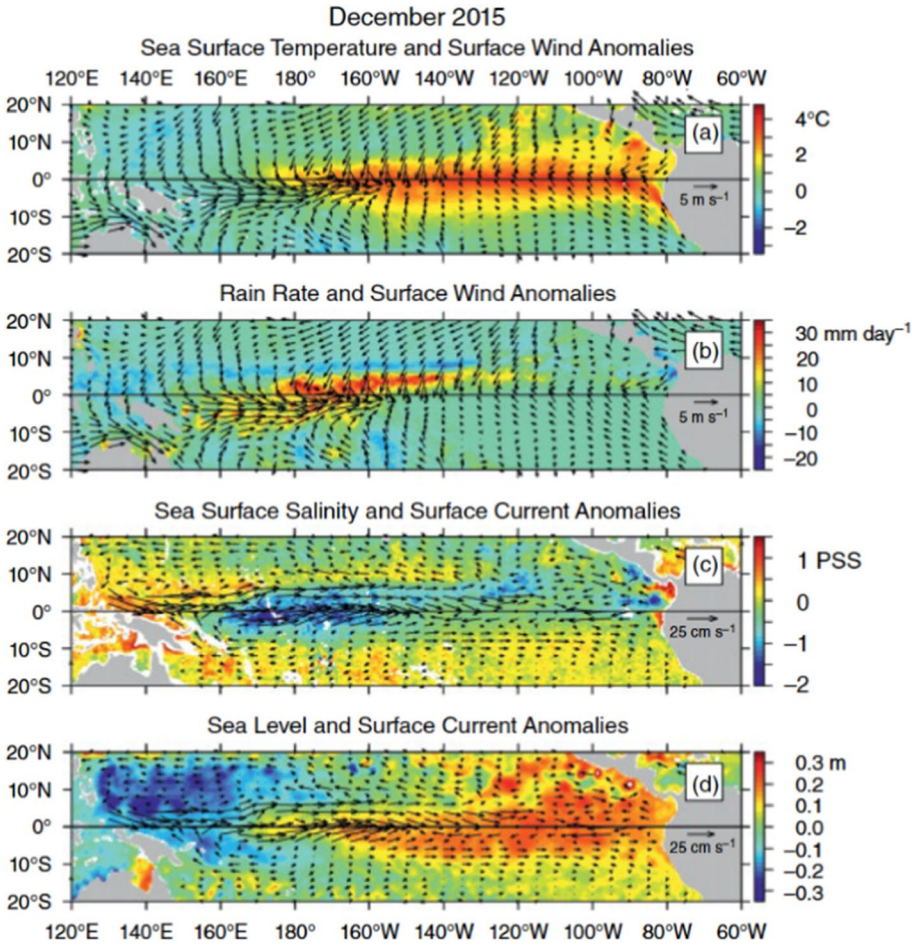

Fig. 1 Satellite-based multi-variate characterization of oceanic and atmospheric anomalies during the peak of the extreme El Niño in 2015 (after McPhaden et al. 2020a). December 2015 anomalies of **a** SST and surface winds, **b** rain rate and surface winds, **c** SSS (from SMOS) and surface currents, and **d** sea level and surface currents. Anomalies are computed relative to a mean seasonal cycle over the period of 1998–2017 for all variables except salinity for which anomalies are computed relative to a seasonal cycle over 2010–2017 (see McPhaden et al. 2020a for datasets references)

Satellite-derived SSS has also elucidated other aspects of ENSO-related large-scale SSS variations. For example, during the peak of the 2015 El Niño, satellite-derived SSS revealed a weak negative SSS anomaly at the latitude range of 15°–25°N across much of the zonal extent of the basin including the Hawaii archipelago (Hasson et al. 2018), which is also shown in Fig. 1c (light green color at 15°–20°N over much of the central basin). No notable pattern of precipitation anomalies at this latitude range (Fig. 1b) was able to explain the pattern of weak negative SSS anomalies. Hasson et al. (2018) attributed the latter to the effect of ocean circulation that spread the precipitation-affected SSS anomalies from the equatorial Pacific toward the north, e.g., through the advection by the northward component of the Ekman currents away from the equatorial zone (also evident in the current vectors in Fig. 1c) and likely the instability of the zonal current system. Qu and Yu (2014) found that an index derived from SSS variability in the southeast tropical Pacific (0°–10°S, 150°–90°W) could distinguish central-Pacific versus eastern-Pacific El Niño events. Large extension of the Eastern-Pacific Fresh Pool was also observed in 2012 and 2015 as a result of the combined effect of precipitation and advection by ocean currents (Guimbard et al. 2017).

The important role of salinity in ENSO forecasts has been recognized using satellite-derived SSS. Zhu et al. (2014) found that realistic salinity field in the initialization of an ENSO forecast model improved the hindcast of the 2007–2008 La Niña. Including satellite-derived SSS in the dataset assimilated for the initializations of two other ENSO forecast models demonstrated the positive impacts in the hindcasts of various ENSO events in the past decade because of the improved representation of the mixed-layer dynamics and subsequent air-sea interaction (Hackert et al. 2020 and references therein).

The IOD, an interannual climate mode originating from ocean–atmosphere interaction in the tropical Indian Ocean and modulated by ENSO, has significant impacts on Indian Ocean rim countries and beyond (Saji et al. 1999). SMOS revealed SSS signature of IOD (Durand et al. 2013) with the maximum SSS variation related to IOD being in the central tropical Indian Ocean south of the Equator. The SSS difference in this region between the periods for the negative (positive) IOD events in late 2010 (2011) reached 1 pss, comparable to the magnitude of SSS anomalies in the central-equatorial Pacific during the 2015 El Niño as shown in Fig. 1c. Horizontal advection by zonal currents in the tropical Indian Ocean was identified as a major cause for such IOD-related maximum SSS variation. Using SMOS and Aquarius SSS data, Du and Zhang (2015) further characterized IOD-related SSS signatures during 2010–2014 and wind-driven ocean dynamics associated with IOD both for the central-equatorial Indian Ocean studied by Durand et al. (2013) and for the coastal ocean off Java and Sumatra where changes in wind-driven upwelling influence SSS in that region. IOD-related wind forcing also causes wave propagation around the Bay of Bengal that modulate the river plume and freshwater exchange between the Bay of Bengal and the Arabian Sea (e.g., Akhil et al. 2020; Fournier et al. 2017b, Nyadjro and Subrahmanyam 2016), which will be discussed in Sect. 4.2 in the context of ocean-water cycle linkages.

On intraseasonal time scales, MJO is the dominant mode of variability in the tropics and influences longer time scales climate variability such as the monsoon and ENSO. Ocean–atmosphere interaction has been suggested to influence MJO development and propagation (DeMott et al. 2015; Lau et al. 2012 and references therein). The evaluation of ocean–atmosphere interactions associated with MJO simulated by models requires measurements of SSS as well as SST with sufficient sampling and coverage to capture the respective signatures associated with MJO. Various studies have demonstrated the ability of satellite SSS to detect MJO-related SSS signature (Shoup et al. 2019 and references

therein). The contribution of SSS variation to surface density variation associated with MJO was found to be comparable to or larger than the contribution of SST variation (Guan et al. 2014). In the western to central tropical Indian Ocean, MJO-related precipitation was found to be the main cause for the related SSS variation. However, ocean dynamics play an important role to MJO-related SSS variations in the eastern tropical Indian Ocean and western tropical Pacific. Such findings provided important observational basis to evaluate ocean circulation models (Li et al. 2015; Zhu et al. 2020). Whether salinity variation associated with MJO affects SST through vertical mixing and thereby influences MJO evolution requires future investigation.

Satellite-derived SSS has also provided important insights to the signatures and dynamics of tropical instability waves (TIWs). TIWs are thousand-km scale oceanic waves associated with oceanic instability but modulated by ocean–atmosphere interactions (e.g., Chelton et al. 2001; Legeckis 1977). They have important effects on ocean dynamics, marine biogeochemistry, and ocean–atmosphere interaction. For the first time, satellite-derived SSS shed light on SSS structure of TIWs in the tropical Pacific and Atlantic Oceans, the dependence of Pacific TIW speed on latitude (Lee et al. 2012) and the phase of ENSO (Yin et al. 2014), and the important roles of salinity in Atlantic energetics (Lee et al. 2014; Olivier et al. 2020).

4.2 SSS and the Water Cycle: Maritime Continent Region, River Plumes

Salinity-measuring satellites have provided an unprecedented capability to study ocean-water cycle linkages (e.g., Reul et al. 2014b; Vinogradova et al. 2019). For example, these measurements have enabled insights about the linkage between water cycle and ocean circulation in the maritime continent (MC) region (Lee et al. 2019), a climatically important sector and a chokepoint of the global ocean circulation connecting the Pacific and Indian Ocean. SMAP and SMOS SSS consistently depicted the spatial pattern and temporal evolution of the seasonal freshening in the Indonesian Seas within the MC associated with local monsoonal rainfall and runoff from the Borneo Island. These features have not been documented from in situ measurements before due to their paucity and heterogeneity. The seasonal freshening results in upper-layer dynamic height or sea level anomaly that reduces the north-to-south pressure gradient driving the upper layer of the Indonesian Throughflow (ITF) through the Makassar Strait (the main channel of the ITF). This modulation of the ITF driving force influences the seasonality and annual-mean vertical profile of the ITF and its associated transports of heat, freshwater, and carbon. The results have strong implications to longer-term changes of the ITF in response to changes of the Walker Circulation and the atmospheric convection and precipitation center over the MC region.

Salinity-measuring satellites have also enabled synoptic mapping of SSS variability of large river plumes, which would not have been achievable with in situ networks alone, and with excellent consistency across SSS products from different satellites (e.g., Boutin et al. 2018; Fournier and Lee 2021; Fournier et al. 2016a; Grodsky and Carton 2018; Grodsky et al. 2014). Large rivers are a key component of the land–ocean branch of the global water and biogeochemical cycles. Although river discharge only accounts for about 10% of the total freshwater input to the ocean (Trenberth et al. 2007), large river plumes can have important influences on physical, biological, and biogeochemical processes in regional coastal oceans. A systematic, routine monitoring of the spatiotemporal variability of these river plumes around the world ocean using in situ sensors is technologically and

logistically challenging, and financially impractical. Salinity-measuring satellites have significantly alleviated this gap, as documented by many recent studies.

For example, Aquarius and SMOS SSS illustrate that interannual variability of SSS near the Mississippi River mouth, linked to the interannual variability of the Mississippi River discharge, can reach 3–4 pss (e.g., Fournier et al. 2016a; Gierach et al. 2013), which is comparable to the magnitude of seasonal SSS variation in the same region. A state-of-the-art global ocean data assimilation product was unable to capture such interannual variation of SSS because the model was forced by climatological seasonal discharge, compounded by the strong relaxation of model SSS to seasonal SSS climatology. Such a model limitation undermines the use of the physical state of such model and data assimilation products to drive marine biogeochemistry models. SMOS SSS revealed an unusual, large river plume in 2015 to the east of the Mississippi River plume that was as strong as the latter (Fournier et al. 2016b) (Fig. 2). The unusual river plume was traced to runoff from the Texas shelf caused by a storm-induced severe flooding event in Texas in May 2015 that caused a freshening of the seawaters off the coast of Texas (Fig. 2a). The low-salinity waters were then carried by ocean currents clockwise around the Gulf and peeled off as a large freshwater plume in the middle of the Gulf by August 2015 (Fig. 2b).

A similarly large river plume occurred multiple times in the Gulf of Mexico since 2015 due to frequent severe storms in the Texas-Louisiana regions, causing mass die-off of marine invertebrates at the marine sanctuary off Texas and Louisiana (https://sanctuaries.noaa.gov/news/jul16/noaa-scientists-report-mass-die-off-of-invertebrates-at-east-flower-garden-bank.html; https://apnews.com/article/65f056630aec4757a5879e0dc6b25691).

Salinity-measuring satellites have also underlined that not all interannual variations of large river plumes are dominated by the effect of interannual river discharge. For example, the spatial extent of the Amazon-Orinoco river plume is significantly affected by the interannual variation of wind-driven ocean dynamics over the western tropical Atlantic (Fournier et al. 2017a; Reverdin et al. 2021). The spatial extent of the Ganges–Brahmaputra river plume along the east coast of India is significantly affected by interannual variation

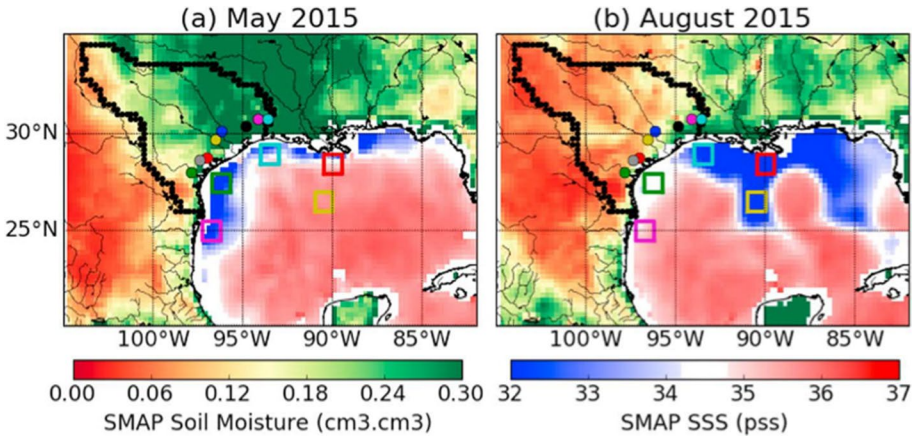

Fig. 2 SSS in the Gulf of Mexico and SM around the Gulf in May (**a**) and August (**b**) 2015 from the SMAP satellite. Adopted from Fournier et al. (2016b). The difference in the pattern of SSS and SM between these two months shows the impact of the severe storm over Texas in May 2015 on SM as well as SSS off the Texas shelf, which subsequently evolved into an unusual and large freshwater plume in the central part of the Gulf

in wind forcing associated with the IOD and the oceanic response (Akhil et al. 2020; Fournier et al. 2017b). Wind-induced currents have also been shown to be one of the main driving forces behind the variability of the Congo region freshwater plume (Hopkins et al. 2013; Houndegnonto et al. 2021). A large interannual variability of the freshwater plumes, related to river discharge but mediated by ocean circulation, has also been observed in the Arctic Ocean (Tarasenko et al. 2021). Such knowledge of how river plumes are linked to the regional hydrological cycle, and climate variability is important for improving the understanding of the interplay among different elements of the Earth system.

Salinity-measuring satellites also provide key information to study the interplay between land-sea fresh water exchange and ocean circulation in the land vicinity. In the core of the saltiest period of the Amazon plume (boreal winter), a freshwater plume was observed to be transported off the shelf, entering the deep north-western tropical Atlantic. According to satellite data, such a phenomenon occurred in 7 out of 10 years, changing the perception that during this period, freshwater transport takes place mainly on the shelf and close to the shelf break (Reverdin et al. 2021). In the Gulf of Guinea, Alory et al. (2021) showed that changes in geostrophic currents and vertical stratification are generated by the Niger River plume and that they weaken the coastal upwelling by about 50% near the mouth of the Niger River. This phenomenon has important consequences on fisheries resources, as the upwellings bring nutrient to the surface.

Satellite SSS has also been used synergistically with other physical and biogeochemical measurements to improve the understanding of how river plumes and the associated effects on near-surface vertical mixing influence primary productivity (Gouveia et al. 2019) and how the associated physical and ecological processes affect marine biogeochemistry (Guerreiro et al. 2017; Lapointe et al. 2021).

4.3 Observing Ocean Thermohaline Fronts from Space

The thermohaline frontal structures and the variability of the ocean are critical for understanding ocean and climate changes, but also for shaping biogeochemical tracers and nutrient distribution, which are fundamental for ecological habitat structuration (Chapman et al. 2020).

Since temperature (salinity) tends to diminish (increase) the density of seawater, the intensity and dynamics of density fronts depend on the strength of temperature and salinity contrasts. They can either cumulate each other to enhance the density contrast, or compensate each other resulting in lower density contrasts. The former will strongly impact the velocity shear, instability and mixing, whereas the latter, for instance at the transition between warm/salty and cool/fresh water, has a very low signature in density gradient. The density compensation behavior is referred to as 'spiciness' (McDougall and Krzysik 2015). Because of the nonlinearity of the equation of state of seawater, the large spiciness contrasts can have a strong impact on water mass generation and transformation. The so-called cabeling process, i.e., mixing of water with contrasted spiciness along a same density surface produces heavier water masses of mixed properties (McDougall 1987; Stewart et al. 2017). These processes can be active along strong spiciness fronts, and can be responsible for generation and subduction of water masses (Thomas and Shakespeare 2015).

As frontal structures are typically mesoscale time and space features, observing and monitoring constantly both temperature and salinity at these scales is not possible with the sampling of in situ historical measurements. Owing to the satellite measurements, both mesoscale SST and SSS fronts can now be monitored simultaneously from space at

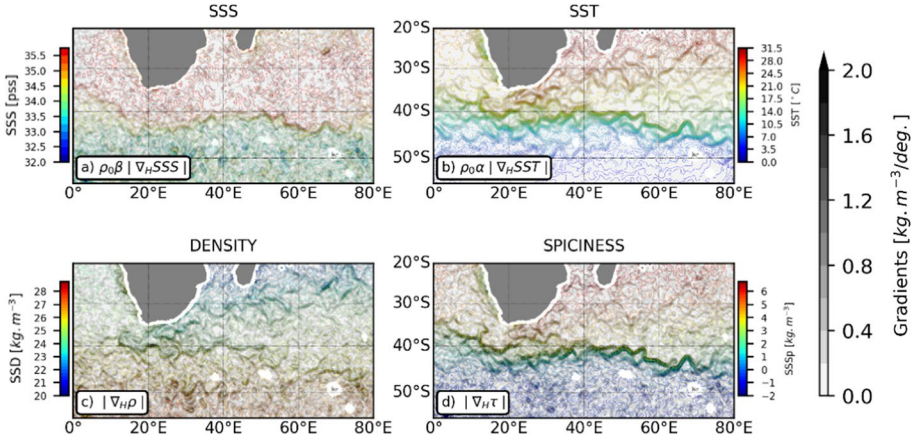

Fig. 3 Subtropical Front in the ocean to the South of South Africa around 10 October 2016. **a** Absolute value of SSS and **b** SST horizontal gradient contribution to **c** SSD gradient and **d** SSSp gradient (gray shading in kg m^{-3}/deg). Corresponding fields of **a** SSS, **b** SST, **c** SSD and **d** SSSp are color contoured

a resolution around 45 km for SSS (and higher resolution for SST), revealing some sharp thermohaline fronts and associated features such as salty eddy and meanders in the Gulf Stream region (Reul et al. 2014a), density compensation in the Azores front and current (Kolodziejczyk et al. 2015), TIW frontal signature (see Sect. 4.1), and large river plume SSS contrasts (see Sect. 4.2).

An example of the thermohaline signature of the Southern Ocean Subtropical Front (STF) in the Southern Indian sector is shown in Fig. 3. The STF is characterized by the sharp horizontal hydrological gradients east of 30°E between 40°S and 45°S (Fig. 3). SST and SSS horizontal gradients (Fig. 3a, b) are computed and dimensionalized as density gradient in order to quantify their respective contribution to SSD and Sea Surface Spiciness (SSSp) gradient (Fig. 3c, d; see Kolodziejczyk et al. (2021), their Eq. 4). SSD and SSSp are computed using TEOS-10 toolbox (IOC et al. 2010), and horizontal SSD and SSSp gradients are then computed.

In the Southern Indian sector, the STF is characterized by the sharp signature in SST and SSS (Fig. 3a, b). Since the Subtropical Fronts are generally the frontiers between cool/fresh subpolar water and warm/salty subtropical waters, these fronts are partly compensated in density. Thus, the spiciness gradient exhibits a very strong signature (Fig. 3d), while density gradient is less marked at mesoscale (Fig. 3c).

This is in sharp contrast with the tropical regions where intense freshwater river discharges and high rain rate produce very high SSS gradients with no compensation in SST. This can create major SSD fronts in the Tropics with potential impacts on local ocean circulation and stratification.

In conclusion, mesoscale fronts analysis from complementary satellite SSS and SST maps has been made possible since 2010, thanks to the launch of L-band radiometric missions. These unprecedented time series reveal the complexity of thermohaline relationship within oceanic fronts on mid- to low latitudes. This will be of greater interest in high latitudes where SSD variability is totally controlled by the SSS gradients, thus with crucial impacts on ocean circulation and mixing processes. However, progress is still needed to improve the resolution (beyond 45 km) and sensitivity (especially in cold water) in SSS

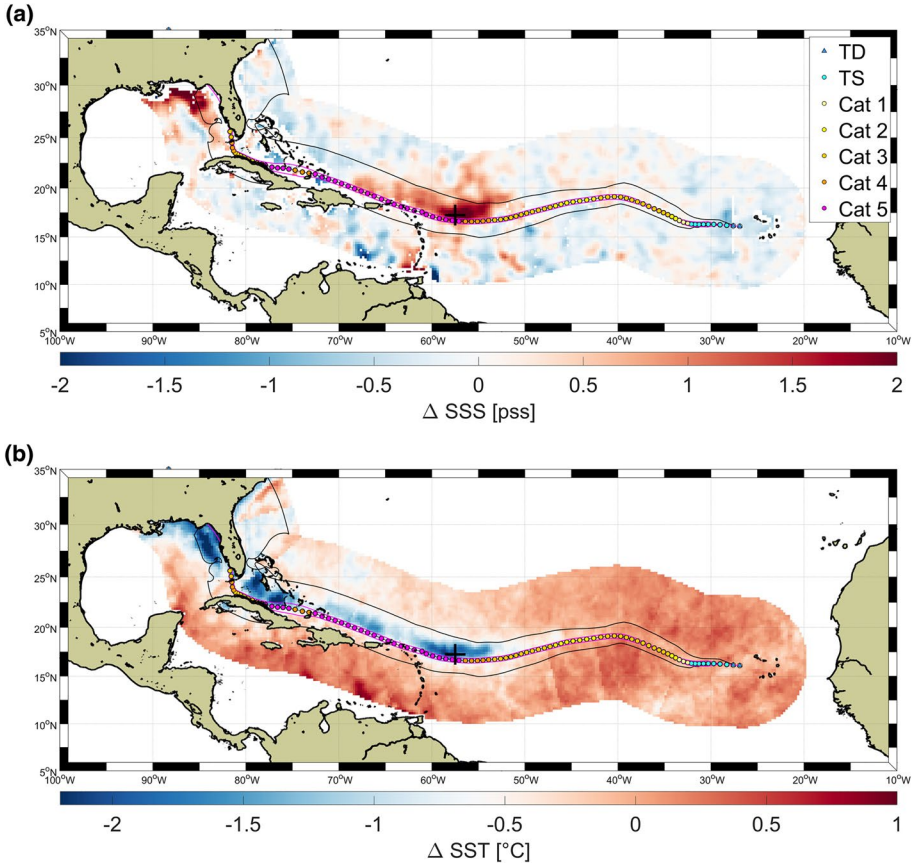

Fig. 4 Sea surface salinity (**a**) and temperature (**b**) response to the passage of category 5 hurricane Irma in the Tropical Atlantic in September 2017. From Reul et al. (2021)

satellite measurements (compared to satellite SST), and to unravel the global dynamical and thermodynamical processes at mesoscale and submesoscale within frontal regions.

4.4 SSS and Tropical Cyclones

Tropical Cyclones (TCs) are strongly influenced by the underlying SST, which in turn is affected by Tropical ocean variability. TCs also typically induce a cold wake of upper-ocean temperatures that can provide a negative feedback, therefore decreasing their intensities.

The strength of the feedback depends on a storm's intensity and translation speed as well as on the ocean heat content and salinity structure, which vary regionally and on seasonal to multidecadal timescales (Balaguru et al. 2012, 2015; Bauer-Marschallinger et al. 2018; Shay et al. 2000). This is especially true in the northwestern tropical Atlantic and Bay of Bengal, where the river plumes (Amazon-Orinoco, Ganga and Brahamaputra) increase salinity stratification, limiting hurricane-induced SST cooling (Balaguru et al. 2012; Domingues et al. 2015; Grodsky et al. 2012; Reul et al. 2014c, 2021).

The climatological impact of TCs on SSS has been recently evaluated for the first time using a decade of satellite SSS observations in Reul et al. (2021) and Sun et al. (2021a). As shown in Fig. 4, TCs act to initially freshen the ocean surface (due to precipitation), and subsequently salinify the surface, largely through vertical ocean processes (mixing and upwelling), with strongest surface salinification on the right-hand side of the Northern Hemisphere TCs.

The direction of vertical wind shear has also been found to control the location of maximum TC rainfall, resulting in more freshwater accumulation on the right-hand side of the right-sheared storms (Sun et al. 2021b). The accumulated freshwater strengthens salinity stratification and inhibits right-side vertical mixing, reducing subsequent surface salinification by 0.15–0.3 pss and slightly reducing the surface cooling by about 0.15 °C, relative to left-sheared storms. Thus, the directionality of shear can impact ocean-TC coupling.

TC rapid intensification (RI) is difficult to predict and poses a formidable threat to coastal populations. A warm upper ocean is well known to favor RI, but the role of ocean salinity is less clear. Balaguru et al. (2020) showed a strong inverse relationship between salinity and TC RI in the eastern Caribbean and western tropical Atlantic due to near-surface freshening from the Amazon–Orinoco River system. The impact of interannual to multidecadal changes in upper-ocean temperature and salinity stratification on TCs' cold wakes and intensities has only begun to be explored (Balaguru et al. 2020; Huang et al. 2015).

5 Perspectives

5.1 Scientific Needs

Both SSS and SM are Essential Climate Variable. SSS is also an Essential Ocean Variable (Buontempo 2022). L-band radiometric missions have provided unique measurements that are crucial to better understand our changing environment and have now accumulated a good track record. Radiometric L-band SSS is the root information used to build the ESA Climate Change Initiative (CCI; https://climate.esa.int) SSS fields (Boutin et al. 2021a, b). Radiometric L-band SM, which provides direct information about surface SM contrary to active measurements influenced by surface roughness and subsurface structure of soil elements, participates to the ESA CCI SM climate data record (Madelon et al. 2021). All this argues in favor of a long time series of L-band radiometric measurements enabling the monitoring of interannual to decadal variability. However, no gap-free continuity is ensured. While SMOS has been operating for more than 13 years and SMAP for almost 8 years, the next mission carrying an L-band radiometer will be either the Chinese Ocean Salinity satellite planned to be launched in 2024 (Li et al. 2022), or the Copernicus Imaging Microwave Radiometer (CIMR) that will not be launched before 2028. Both missions will provide multi-variables (e.g., SST, wind/roughness, SSS, ice parameters) that are helpful for SSS retrieval and for process studies, but with a similar or even a coarser spatial resolution at L-band than SMOS and SMAP. No SMOS follow-on interferometric mission is planned even though a number of SM and SSS applications, e.g., for monitoring fronts where key processes take place (see Sect. 4.3), for improving SSS monitoring close to coast (see Sect. 4.2), would need higher spatial resolution that can only be provided by the interferometric technique.

5.2 The Copernicus Imaging Microwave Radiometer (CIMR) Mission

CIMR is a satellite system developed as part of the European Union Copernicus program expansion activities. CIMR is designed to monitor the rapid Earth system changes taking place in the Arctic in response to the Integrated European Policy for the Arctic requirements (Donlon 2020). The aim of the mission is to provide high-spatial resolution microwave imaging radiometry measurements and derived products with global coverage and sub-daily revisit in the polar regions and adjacent seas to address Copernicus user needs. Its main challenges are (1) to provide high spatial resolution 5 km Ka/Ku band measurements of sea ice parameters (Sea Ice Concentration, Sea Ice Drift, Sea Ice Thickness, Snow Depth on sea ice and Sea Ice Surface Temperature), which provides an enhanced capability compared to 89 GHz estimates that are challenged by atmospheric effects. Other key objectives are (2) to provide high spatial resolution (15 km) C/X band measurements of global coverage SST with quasi all-weather capability and rapid (1–2 days) revisit, and (3) to maintain an L-band measurement capability to continue the legacy of SSS and SM parameters from previous L-band missions but with a coarser spatial resolution. The CIMR instrument concept is based around a conically scanning multi-frequency microwave radiometer with a 55° incidence angle with the Earth surface. CIMR measurements will be made using a forward scan arc followed by a second measurement of the same location using a backward scan arc 260 s later. Channels in L, C, X, Ku, and Ka bands, centered at 1.414, 6.925, 10.65, 18.7 and 36.5 GHz, respectively, are included in the mission design. The measurements will be acquired in vertical (V) and horizontal (H) polarizations, with on board and on ground strategies put in place to mitigate RFI contamination. Modified Stokes parameters will be computed on-board the spacecraft. The spatial resolution of the real-aperture antenna for the C/X-band channel is at least 15 km, and 5 and 4 km for the Ku and Ka-band channels, respectively. The L-band channel will have a real-aperture resolution of at best 60 km (instantaneous, i.e., without accounting for smearing), fundamentally limited by the size of the reflector and the focus of the L-band feed. However, all channels will be oversampled along and across-track by 20% allowing gridded products to be generated at better spatial resolutions. Channel Noise Equivalent Delta Temperature (NEDT) is 0.2–0.7 K with total standard uncertainty at processing Level L1B (instrument data processed to sensor units) better than 0.5 K (L, C, X), 0.6 K (Ku), and 0.7 K (Ka). Recent evaluations of the CIMR retrieval performances (Jiménez et al. 2021; Kilic et al. 2021) showed that the simulated CIMR instrument shall provide SSS with accuracy < 0.3 pss for monthly average composite at spatial resolution ~ 50 km, conforming with the mission requirements (Donlon 2020).

5.3 Active Systems

Contrary to passive microwave radiometry, active systems are very sensitive to subsurface soil structure and water distribution, flawing SM estimates [e.g., (Wagner et al. 2022)]. Nevertheless, they complement radiometric SM estimates by providing higher resolution information (cf Sect. 2.2).

The advent of future L-band missions such as NISAR and ROSE-L, which are planned to be launched in 2024 and 2028, respectively, should improve SAR SM estimates, especially in the context of high vegetation density where C-band measurements are restricted to less penetration of vegetation cover. Radar multifrequency synergies, as well as spatial

multiresolution data, offer an excellent opportunity for more precise SM products at the scale of agricultural plots.

The GNSS networks are being rapidly expanded by multiple nations, and the total number of GNSS satellites operating at L-band frequencies may reach 100 or more soon, which can be source of the L-band reflectometry for SM sensing. A temporal revisit of 1 h or less could be within reach.

The L-band radiometry and GNSS-R missions can provide insights into near-surface SM storage, but do not provide direct information about RZSM, which plays a key role in the evapotranspiration/latent heat flux to the atmosphere and the modulation of recharge to near-surface groundwater aquifers. Therefore, there have been increasing interests to leverage the reflectometry technology to lower frequency by using the signals from communication satellites such as the Navy's Mobile Users Objective System (MUOS) operating at P-band frequencies (Oetting and Jen 2011). The sensitivity of the P-band reflection signals to SM has been analyzed theoretically in Garrison et al. (2017) and Xu et al. (2017) and has been demonstrated in Yueh et al. (2020a). To mature the spaceborne P-band reflectometry technology, the NASA InVEST program has selected the SigNals of Opportunity: P-Band Investigation (SNOOPI) mission (Garrison et al. 2019), which will enable the flight demonstration of the P-Cion host board design. A spaceborne concept, which utilizes the synthetic aperture radar processing approach and combines the signals from an array of small satellites with parallel ground tracks, has been under development in order to reach a spatial resolution of about 100 m to 1 km (Yueh et al. 2021). Nevertheless, the P-band is not an RFI protected band contrary to L-band, and the feasibility of such measures over most of the land surface remains to be demonstrated.

5.4 SMOS-HR

SMOS, Aquarius and SMAP have demonstrated the uniqueness and usefulness of L-band radiometry. Capitalizing on the successes of these missions, acquiring such measurements should continue, especially in view of the many operational and scientific users. Obviously, data gaps would be most compromising. Several studies and workshops were thus held to address this issue while various technology demonstrators were developed. Several summary notes on these activities were produced (Kerr et al. 2019a, b) and presented to the scientific community (Kerr et al. 2020). On land, the need for high spatial resolution for SM is obvious, and radiometric measurements are unique in providing reference SM values. Over ocean, studies increasingly point to the strong need for a significant improvement of the spatial resolution. For instance, D'Addezio et al. (2019) found that with 40 km resolution measurements, about 30% of the total SSS variance within 640 km scale is missed, whereas the missing variance is only 5% with 10 km resolution measurements. In tropical regions, the importance of oceanic mesoscale in the export of freshwater and carbon from river plumes has been studied using SMOS and SMAP SSS, but many finer scale phenomena revealed by high-resolution chlorophyll-a, but not accessible with current L-band radiometers, highlight the need for high-resolution satellite salinity (Olivier et al. 2022). Moreover, an improved quantification of salt transport by eddies that plays a major role in balancing evaporation and precipitation fluxes requires improved resolution capabilities of future satellite missions in order to observe mesoscale and sub-mesoscale variability, improving the signal-to-noise ratio, and extending these capabilities to polar oceans (Melnichenko et al. 2021). Especially since in the Arctic Ocean, current satellite measurements have shown the potential of L-band radiometry to track the spatio-temporal evolution of

Table 2 Trade offs for the requirements of a near future mission

Spatial resolution	10 km
Temporal resolution	3 days on the Equator (would be better at higher latitudes)
Radiometric accuracy	0.5 K

freshwater from melting ice, but also their severe lack of spatial resolution (Supply et al. 2022).

Some key high-level system requirements detailed in the studies previously mentioned are summarized below, and trade offs for the requirements for a near future mission are summarized in Table 2.

Spatial resolution should be at the very least as good as that of SMOS and SMAP, and ideally 1 km, though at 10 km a significant step forward would already be achieved. The temporal resolution should be at least that of SMOS and SMAP, ideally twice a day. The radiometric accuracy should be at least that of SMAP for a single view, and ideally 0.1 K though 0.5 or even 1 K would satisfy most users.

Other general requirements for ideal follow-on missions are to be fully polarimetric and to have a good RFI filtering approach, as demonstrated by SMAP.

For weather and climate, global coverage should be ensured, while for some operational uses (e.g., NWP, flood forecasts, high winds) a near real-time acquisition is absolutely necessary.

As described above the most challenging issue is to achieve a better spatial resolution, ideally 1 km or less. This seems unachievable with classical antennas since the antenna size and number of receivers grow to an unachievable limit (O'Neill et al. 2018). The solution lies with interferometry as demonstrated by radio astronomers and as proven in space with SMOS (Kerr et al. 2010).

From these considerations, the SMOS–HR concept (now in a phase A study at CNES) was developed. The concept is based on the SMOS heritage with adaptations making the requirements described above achievable (Rodriguez-Fernandez 2020). It capitalizes also on new patented approaches to reach the 10 km spatial resolution with longer arms. The concept also reduces the area of the field of view affected by aliases. A sophisticated RFI filtering approach is also being implemented.

6 Concluding Remarks

Monitoring SSS from space has become possible since 2010 thanks to L-band radiometry. It is still the only spaceborne technique allowing SSS measurements. The space measurement of SM was first initiated by active technique (scatterometry) but active measurements are also at first-order sensitive to the surface roughness and to the distribution of elements in the soil. Only L-band radiometry provides access, since 2010, to direct SM measurements. SM derived from L-band radiometric measurements is now used as a reference for adjusting large-scale SM determined by active methods. Thanks to recent technological advances (SAR, reflectometry), the great benefit of the latter is to provide information about the SM variability at the kilometer scale, or even smaller, while the spatial resolution reached by L-band radiometers currently in flight is ~43 km. Maintaining a good knowledge of the SSS and SM therefore necessitates the continuity of L-band radiometric

measurements. The Chinese Ocean Salinity mission and CIMR are expected to carry the next L-band radiometers with spatial resolution of the order of, or coarser than, current measurements, respectively, with an asset of multiple frequencies. But their launch might take place too late to ensure continuity (SMOS and SMAP are the only instruments still in flight for more than 13 years and 8 years, respectively). On the other hand, improving the monitoring of areas and processes that are highly sensitive to climate change, near the coasts, near the ice, and near inhabited land areas requires an improved spatial resolution. Development of new technological concepts opens the way to a spatial resolution of the order of ten kilometers or less.

Acknowledgements We thank three anonymous reviewers for their insightful remarks. We are indebted to Audine Laurian for her careful rereading of a draft of this document.

References

Akbar R, Short Gianotti D, McColl KA, Haghighi E, Salvucci GD, Entekhabi D (2018) Hydrological storage length scales represented by remote sensing estimates of soil moisture and precipitation. Water Resour Res 54(3):1476–1492. https://doi.org/10.1002/2017WR021508

Akhil VP, Vialard J, Lengaigne M, Keerthi MG, Boutin J, Vergely JL, Papa F (2020) Bay of Bengal Sea surface salinity variability using a decade of improved SMOS re-processing. Remote Sens Environ 248:111964. https://doi.org/10.1016/j.rse.2020.111964

Al-Khaldi MM, Johnson JT, O'Brien AJ, Balenzano A, Mattia F (2019) Time-series retrieval of soil moisture using CYGNSS. IEEE Trans Geosci Remote Sens 57(7):4322–4331. https://doi.org/10.1109/TGRS.2018.2890646

Alory G, Da-Allada CY, Djakouré S, Dadou I, Jouanno J, Loemba DP (2021) Coastal upwelling limitation by onshore geostrophic flow in the gulf of guinea around the niger river plume. Front Mar Sci 7:1116. https://doi.org/10.3389/fmars.2020.607216

Amazirh A, Merlin O, Er-Raki S (2019) Including Sentinel-1 radar data to improve the disaggregation of MODIS land surface temperature data. ISPRS J Photogramm Remote Sens 150:11–26. https://doi.org/10.1016/J.ISPRSJPRS.2019.02.004

Baghdadi N, Zribi M (2016) Microwave remote sensing of land surfaces: techniques and methods. ISTE Press. https://doi.org/10.1016/C2016-0-00232-2

Balaguru K, Chang P, Saravanan R, Leung LR, Xu Z, Li M, Hsieh J-S (2012) Ocean barrier layers' effect on tropical cyclone intensification. Proc Natl Acad Sci 109(36):14343–14347. https://doi.org/10.1073/pnas.1201364109

Balaguru K, Foltz GR, Leung LR, Asaro ED, Emanuel KA, Liu H, Zedler SE (2015) Dynamic Potential Intensity: an improved representation of the ocean's impact on tropical cyclones. Geophys Res Lett 42(16):6739–6746. https://doi.org/10.1002/2015GL064822

Balaguru K, Foltz GR, Leung LR, Kaplan J, Xu W, Reul N, Chapron B (2020) Pronounced impact of salinity on rapidly intensifying tropical cyclones. Bull Am Meteorol Soc 101(9):E1497–E1511. https://doi.org/10.1175/BAMS-D-19-0303.1

Bauer-Marschallinger B, Freeman V, Cao S, Paulik C, Schaufler S, Stachl T, Modanesi S, Massari C, Ciabatta L, Brocca L (2018) Toward global soil moisture monitoring with Sentinel-1: harnessing assets and overcoming obstacles. IEEE Trans Geosci Remote Sens 57(1):520–539. https://doi.org/10.1109/TGRS.2018.2858004

Baugh C, de Rosnay P, Lawrence H, Jurlina T, Drusch M, Zsoter E, Prudhomme C (2020) The impact of SMOS soil moisture data assimilation within the operational global flood awareness system (GloFAS). Remote Sens. https://doi.org/10.3390/rs12091490

Bindlish R, Barros AP (2000) Multifrequency soil moisture inversion from SAR measurements with the use of IEM. Remote Sens Environ 71(1):67–88. https://doi.org/10.1016/S0034-4257(99)00065-6

Bousquet E, Mialon A, Rodriguez-Fernandez N, Mermoz S, Kerr Y (2022) Monitoring post-fire recovery of various vegetation biomes using multi-wavelength satellite remote sensing. Biogeosciences 19(13):3317–3336. https://doi.org/10.5194/bg-19-3317-2022

Boutin J, Martin N, Yin X, Font J, Reul N, Spurgeon P (2012) First assessment of SMOS data over open ocean: part II—sea surface salinity. IEEE Trans Geosci Remote Sens 50(5):1662–1675. https://doi.org/10.1109/TGRS.2012.2184546

Boutin J, Chao Y, Asher WE, Delcroix T, Drucker R, Drushka K, Kolodziejczyk N, Lee T, Reul N, Reverdin G, Schanze J, Soloviev A, Yu L, Anderson J, Brucker L, Dinnat E, Santos-Garcia A, Jones WL, Maes C, Meissner T, Tang W, Vinogradova N, Ward B (2016) Satellite and in situ salinity: understanding near-surface stratification and subfootprint variability. Bull Am Meteorol Soc 97(8):1391–1407. https://doi.org/10.1175/bams-d-15-00032.1

Boutin J, Vergely JL, Marchand S, D'Amico F, Hasson A, Kolodziejczyk N, Reul N, Reverdin G, Vialard J (2018) New SMOS Sea Surface Salinity with reduced systematic errors and improved variability. Remote Sens Environ 214:115–134. https://doi.org/10.1016/j.rse.2018.05.022

Boutin J, Reul N, Koehler J, Martin A, Catany R, Guimbard S, Rouffi F, Vergely JL, Arias M, Chakroun M, Corato G, Estella-Perez V, Hasson A, Josey S, Khvorostyanov D, Kolodziejczyk N, Mignot J, Olivier L, Reverdin G, Stammer D, Supply A, Thouvenin-Masson C, Turiel A, Vialard J, Cipollini P, Donlon C, Sabia R, Mecklenburg S (2021a) Satellite-based sea surface salinity designed for ocean and climate studies. J Geophys Res Oceans 126(11):e2021JC017676. https://doi.org/10.1029/2021JC017676

Boutin J, Vergely J-L, Dinnat EP, Waldteufel P, D'Amico F, Reul N, Supply A, Thouvenin-Masson C (2021b) Correcting sea surface temperature spurious effects in salinity retrieved from spaceborne L-band radiometer measurements. IEEE Trans Geosci Remote Sens 59(9):7256–7269. https://doi.org/10.1109/tgrs.2020.3030488

Brandt M, Wigneron JP, Chave J, Tagesson T, Penuelas J, Ciais P, Rasmussen K, Tian F, Mbow C, Al-Yaari A, Rodriguez-Fernandez N, Schurgers G, Zhang WM, Chang JF, Kerr Y, Verger A, Tucker C, Mialon A, Rasmussen LV, Fan L, Fensholt R (2018a) Satellite passive microwaves reveal recent climate-induced carbon losses in African drylands. Nat Ecol Evol 2(5):827–835. https://doi.org/10.1038/s41559-018-0530-6

Brandt M, Yue YM, Wigneron JP, Tong XW, Tian F, Jepsen MR, Xiao XM, Verger A, Mialon A, Al-Yaari A, Wang KL, Fensholt R (2018b) Satellite-observed major greening and biomass increase in South China Karst during recent decade. Earths Future 6(7):1017–1028. https://doi.org/10.1029/2018ef000890

C. Buontempo AJHD, Krug T, Schmetz J, Speich S, Thorne P, Zemp M (2022) The 2022 GCOS implementation plan (GCOS-244), report, WMO

Chaparro D, Piles M, Vall-llossera M, Camps A (2016) Surface moisture and temperature trends anticipate drought conditions linked to wildfire activity in the Iberian Peninsula. Eur J Remote Sens 49(1):955–971. https://doi.org/10.5721/EuJRS20164950

Chapman CC, Lea M-A, Meyer A, Sallée J-B, Hindell M (2020) Defining Southern Ocean fronts and their influence on biological and physical processes in a changing climate. Nat Clim Change 10(3):209–219. https://doi.org/10.1038/s41558-020-0705-4

Chelton DB, Esbensen SK, Schlax MG, Thum N, Freilich MH, Wentz FJ, Gentemann CL, McPhaden MJ, Schopf PS (2001) Observations of coupling between surface wind stress and sea surface temperature in the eastern tropical Pacific. J Clim 14(7):1479–1498. https://doi.org/10.1175/1520-0442(2001)014%3c1479:OOCBSW%3e2.0.CO;2

Chew C, Small E (2018) Soil moisture sensing using spaceborne GNSS reflections: comparison of CYGNSS reflectivity to SMAP soil moisture. Geophys Res Lett 45(9):4049–4057. https://doi.org/10.1029/2018GL077905

Choudhury BJ, Schmugge TJ, Chang A, Newton RW (1979) Effect of surface roughness on the microwave emission from soils. J Geophys Res Oceans 84(C9):5699–5706. https://doi.org/10.1029/JC084iC09p05699

Clarizia MP, Pierdicca N, Costantini F, Floury N (2019) Analysis of CYGNSS data for soil moisture retrieval. IEEE J Sel Top Appl Earth Observ Remote Sens 12(7):2227–2235. https://doi.org/10.1109/JSTARS.2019.2895510

Colliander A, Ruokokoski L, Suomela J, Veijola K, Kettunen J, Kangas V, Aalto A, Levander M, Greus H, Hallikainen MT, Lahtinen J (2007) Development and calibration of SMOS reference radiometer. IEEE Trans Geosci Remote Sens 45(7):1967–1977. https://doi.org/10.1109/TGRS.2007.894055

Colliander A, Reichle R, Crow W, Cosh M, Chen F, Chan S, Das N, Bindlish R, Chaubell J, Kim S, Liu Q, O'Neill P, Dunbar S, Dang L, Kimball J, Jackson T, AlJassar H, Asanuma J, Bhattacharya B, Berg A, Bosch D, Bourgeau-Chavez L, Caldwell T, Calvet J-C, Collins CH, Jensen K, Livingston S, López-Baeza E, Martínez-Fernández J, McNairn H, Moghaddam M, Montzka C, Notarnicola C, Pellarin T, Pfeil I, Pulliainen J, Ramos J, Seyfrie M, Starks P, Su Z, Thibeault M, van der Velde R, Vreugdenhil M, Walker J, Zeng Y, Zribi M, Entekhabi D, Yueh S (2021) Validation of soil moisture data products from the NASA SMAP mission. IEEE J Sel Top Appl Earth Observ Remote Sens 15:364–392. https://doi.org/10.1109/JSTARS.2021.3124743

Crow WT, Gomez CA, Sabater JM, Holmes T, Hain CR, Lei FN, Dong JZ, Alfieri JG, Anderson MC (2020) Soil moisture-evapotranspiration overcoupling and L-band brightness temperature assimilation: sources and forecast implications. J Hydrometeorol 21(10):2359–2374. https://doi.org/10.1175/jhm-d-20-0088.1

D'Addezio JM, Bingham FM, Jacobs GA. (2019) Sea surface salinity subfootprint variability estimates from regional high-resolution model simulations. Remote Sens Environ. https://doi.org/10.1016/j.rse.2019.111365

Daganzo-Eusebio E, Oliva R, Kerr YH, Nieto S, Richaume P, Mecklenburg SM (2013) SMOS Radiometer in the 1400–1427-MHz passive band: impact of the RFI environment and approach to its mitigation and cancellation. IEEE Trans Geosci Remote Sens 51(10):4999–5007. https://doi.org/10.1109/TGRS.2013.2259179

Dari J, Quintana-Segui P, Escorihuela MJ, Stefan V, Brocca L, Morbidelli R (2021) Detecting and mapping irrigated areas in a Mediterranean environment by using remote sensing soil moisture and a land surface model. J Hydrol 596:126129. https://doi.org/10.1016/j.jhydrol.2021.126129

DeMott CA, Klingaman NP, Woolnough SJ (2015) Atmosphere-ocean coupled processes in the Madden-Julian oscillation. Rev Geophys 53(4):1099–1154. https://doi.org/10.1002/2014RG000478

Domingues R, Goni G, Bringas F, Lee S-K, Kim H-S, Halliwell G, Dong J, Morell J, Pomales L (2015) Upper ocean response to Hurricane Gonzalo (2014): Salinity effects revealed by targeted and sustained underwater glider observations. Geophys Res Lett 42(17):7131–7138. https://doi.org/10.1002/2015GL065378

Dong J, Crow WT (2018) Use of satellite soil moisture to diagnose climate model representations of European soil moisture-air temperature coupling strength. Geophys Res Lett 45(23):12884–12891. https://doi.org/10.1029/2018GL080547

Donlon CJ (2020) The copernicus imaging microwave radiometer (CIMR) mission requirements document, v4.0. https://esamultimedia.esa.int/docs/EarthObservation/CIMR-MRD-v4.0-20201006_Issued.pdf

Du Y, Zhang Y (2015) Satellite and argo observed surface salinity variations in the tropical indian ocean and their association with the Indian Ocean Dipole mode. J Clim 28(2):695–713. https://doi.org/10.1175/jcli-d-14-00435.1

Durand F, Alory G, Dussin R, Reul N (2013) SMOS reveals the signature of Indian Ocean Dipole events. Ocean Dyn 63(11):1203–1212. https://doi.org/10.1007/s10236-013-0660-y

El Hajj M, Baghdadi N, Zribi M, Bazzi H (2017) Synergic use of sentinel-1 and sentinel-2 images for operational soil moisture mapping at high spatial resolution over agricultural areas. Remote Sens 9(12):1292. https://doi.org/10.3390/rs9121292

English S, Prigent C, Johnson B, Yueh S, Dinnat E, Boutin J, Newman S, Anguelova M, Meissner T, Kazumori M, Weng F, Supply A, Kilic L, Bettenhausen M, Stoffelen A, Accadia C (2020) Reference-quality emission and backscatter modeling for the ocean. Bull Am Meteor Soc 101(10):E1593–E1601. https://doi.org/10.1175/bams-d-20-0085.1

Entekhabi D, Njoku EG, Neill PEO, Kellogg KH, Crow WT, Edelstein WN, Entin JK, Goodman SD, Jackson TJ, Johnson J, Kimball J, Piepmeier JR, Koster RD, Martin N, McDonald KC, Moghaddam M, Moran S, Reichle R, Shi JC, Spencer MW, Thurman SW, Tsang L, Zyl JV (2010) The Soil Moisture Active Passive (SMAP) mission. Proc IEEE 98(5):704–716. https://doi.org/10.1109/JPROC.2010.2043918

Entekhabi D, Yueh SH, Oneill PE, Kellogg KH, Allen AM, Bindlish R, Brown ME, Chan STK, Colliander A, Crow WT, Das NN, Lannoy GD, Dunbar RS, Edelstein WN, Entin JK, Escobar VM, Goodman SD, Jackson TJ, Jai B, Johnson JT, Kim EJ, Kim S, Kimball JS, Koster RD, Leon A, McDonald K, Moghaddam M, Mohammed PN, Moran S, Njoku EG, Piepmeier JR, Reichle RH, Rogez F, Shi J, Spencer MW, Thurman SW, Tsang L, Zyl JJV, Weiss BH, West RD (2014) SMAP handbook-soil moisture active passive: mapping soil moisture and freeze/thaw from space. https://smap.jpl.nasa.gov/files/smap2/SMAP_Handbook_FINAL_1_JULY_2014_Web.pdf

Eroglu O, Kurum M, Boyd D, Gurbuz AC (2019) High spatio-temporal resolution CYGNSS soil moisture estimates using artificial neural networks. Remote Sens 11(19):2272. https://doi.org/10.3390/rs11192272

Escorihuela MJ, Merlin O, Stefan V, Moyano G, Eweys OA, Zribi M, Kamara S, Benahi AS, Ebbe MAB, Chihrane J, Ghaout S, Cissé S, Diakité F, Lazar M, Pellarin T, Grippa M, Cressman K, Piou C (2018) SMOS based high resolution soil moisture estimates for desert locust preventive management. Remote Sens Appl Soc Environ 11:140–150. https://doi.org/10.1016/j.rsase.2018.06.002

Ezzahar J, Ouaadi N, Zribi M, Elfarkh J, Aouade G, Khabba S, Er-Raki S, Chehbouni A, Jarlan L (2020) Evaluation of backscattering models and support vector machine for the retrieval of bare soil moisture from Sentinel-1 data. Remote Sens 12(1):72. https://doi.org/10.3390/rs12010072

Fan L, Wigneron JP, Xiao Q, Al-Yaari A, Wen J, Martin-StPaul N, Dupuy JL, Pimont F, Al Bitar A, Fernandez-Moran R, Kerr YH (2018) Evaluation of microwave remote sensing for monitoring live fuel moisture content in the Mediterranean region. Remote Sens Environ 205:210–223. https://doi.org/10.1016/j.rse.2017.11.020

Feldman AF, Short Gianotti DJ, Trigo IF, Salvucci GD, Entekhabi D (2019) Satellite-based assessment of land surface energy partitioning-soil moisture relationships and effects of confounding variables. Water Resour Res 55(12):10657–10677. https://doi.org/10.1029/2019WR025874

Fleischmann AS, Al Bitar A, Oliveira AM, Siqueira VA, Colossi BR, Paiva R, Kerr Y, Ruhoff A, Fan FM, Pontes PRM, Collischonn W (2021) Synergistic calibration of a hydrological model using discharge and remotely sensed soil moisture in the Parana River Basin. Remote Sens. https://doi.org/10.3390/rs13163256

Ford TW, Harris E, Quiring SM (2014) Estimating root zone soil moisture using near-surface observations from SMOS. Hydrol Earth Syst Sci 18(1):139–154. https://doi.org/10.5194/hess-18-139-2014

Foucras M, Zribi M, Albergel C, Baghdadi N, Calvet J-C, Pellarin T (2020) Estimating 500-m resolution soil moisture using Sentinel-1 and optical data synergy. Water 12(3):866. https://doi.org/10.3390/w12030866

Fournier S, Lee T (2021) Seasonal and interannual variability of sea surface salinity near major river mouths of the world ocean inferred from gridded satellite and in-situ salinity products. Remote Sens 13(4):728. https://doi.org/10.3390/rs13040728

Fournier S, Lee T, Gierach MM (2016a) Seasonal and interannual variations of sea surface salinity associated with the Mississippi River plume observed by SMOS and Aquarius. Remote Sens Environ 180:431–439. https://doi.org/10.1016/j.rse.2016.02.050

Fournier S, Reager J, Lee T, Vazquez-Cuervo J, David C, Gierach M (2016b) SMAP observes flooding from land to sea: the Texas event of 2015. Geophys Res Lett 43(19):10338–10346. https://doi.org/10.1002/2016GL070821

Fournier S, Vandemark D, Gaultier L, Lee T, Jonsson B, Gierach MM (2017a) Interannual variation in offshore advection of Amazon-Orinoco plume waters: Observations, forcing mechanisms, and impacts. J Geophys Res Oceans 122(11):8966–8982. https://doi.org/10.1002/2017JC013103

Fournier S, Vialard J, Lengaigne M, Lee T, Gierach MM, Chaitanya AVS (2017b) Modulation of the Ganges-Brahmaputra river plume by the Indian Ocean Dipole and eddies inferred from satellite observations. J Geophys Res Oceans 122(12):9591–9604. https://doi.org/10.1002/2017JC013333

Gao Q, Zribi M, Escorihuela MJ, Baghdadi N (2017) Synergetic use of Sentinel-1 and Sentinel-2 data for soil moisture mapping at 100 m resolution. Sensors 17(9):1966. https://doi.org/10.3390/s17091966

Garrison J, Lin YC, Nold B, Piepmeier JR, Vega MA, Fritts M, Toit CFD, Knuble J (2017) Remote sensing of soil moisture using P-band signals of opportunity (SoOp): initial results. In: 2017 IEEE international geoscience and remote sensing symposium (IGARSS), pp 4158–4161. https://doi.org/10.1109/IGARSS.2017.8127917

Garrison JL, Piepmeier J, Shah R, Vega MA, Spencer DA, Banting R, Firman CM, Nold B, Larsen K, Bindlish R (2019) SNOOPI: a technology validation mission for P-band reflectometry using signals of opportunity. In: IGARSS 2019—2019 IEEE international geoscience and remote sensing symposium, pp 5082–5085. https://doi.org/10.1109/IGARSS.2019.8900351

Gherboudj I, Beegum SN, Marticorena B, Ghedira H (2015) Dust emission parameterization scheme over the MENA region: sensitivity analysis to soil moisture and soil texture. J Geophys Res Atmos 120(20):10,915-10,938. https://doi.org/10.1002/2015JD023338

Gianotti DJ, Rigden AJ, Salvucci GD, Entekhabi D (2019a) Satellite and station observations demonstrate water availability's effect on continental-scale evaporative and photosynthetic land surface dynamics. Water Resour Res 55(1):540–554. https://doi.org/10.1029/2018WR023726

Gianotti DJ, Salvucci GD, Akbar R, McColl KA, Cuenca R, Entekhabi D (2019b) Landscape water storage and subsurface correlation from satellite surface soil moisture and precipitation observations. Water Resour Res 55(11):9111–9132. https://doi.org/10.1029/2019WR025332

Gibon F, Pellarin T, Román-Cascón C, Alhassane A, Traoré S, Kerr Y, Chong LS, Baron D, C. (2018) Millet yield estimates in the Sahel using satellite derived soil moisture time series. Agric for Meteorol 262(15 November 2018):100–109. https://doi.org/10.1016/j.agrformet.2018.07.001

Gierach MM, Vazquez-Cuervo J, Lee T, Tsontos VM (2013) Aquarius and SMOS detect effects of an extreme Mississippi River flooding event in the Gulf of Mexico. Geophys Res Lett 40(19):5188–5193. https://doi.org/10.1002/grl.50995

Gouveia NA, Gherardi DFM, Wagner FH, Paes ET, Coles VJ, Aragão LEOC (2019) The salinity structure of the Amazon river plume drives spatiotemporal variation of oceanic primary productivity. J Geophys Res Biogeosci 124(1):147–165. https://doi.org/10.1029/2018JG004665

Grodsky SA, Carton JA (2018) Delayed and quasi-synchronous response of tropical Atlantic surface salinity to rainfall. J Geophys Res Oceans 123(8):5971–5985. https://doi.org/10.1029/2018JC013915

Grodsky SA, Reul N, Lagerloef G, Reverdin G, Carton JA, Chapron B, Quilfen Y, Kudryavtsev VN, Kao H-Y (2012) Haline hurricane wake in the Amazon/Orinoco plume: AQUARIUS/SACD and SMOS observations. Geophys Res Lett 39(20):25. https://doi.org/10.1029/2012GL053335

Grodsky SA, Reverdin G, Carton JA, Coles VJ (2014) Year-to-year salinity changes in the Amazon plume: contrasting 2011 and 2012 Aquarius/SACD and SMOS satellite data. Remote Sens Environ 140:14–22. https://doi.org/10.1016/j.rse.2013.08.033

Guan B, Lee T, Halkides DJ, Waliser DE (2014) Aquarius surface salinity and the Madden-Julian Oscillation: the role of salinity in surface layer density and potential energy. Geophys Res Lett 41(8):2858–2869. https://doi.org/10.1002/2014GL059704

Guerreiro CV, Baumann KH, Brummer GJA, Fischer G, Korte LF, Merkel U, Sá C, de Stigter H, Stuut JBW (2017) Coccolithophore fluxes in the open tropical North Atlantic: influence of thermocline depth, Amazon water, and Saharan dust. Biogeosciences 14(20):4577–4599. https://doi.org/10.5194/bg-14-4577-2017

Guimbard S, Reul N, Chapron B, Umbert M, Maes C (2017) Seasonal and interannual variability of the Eastern Tropical Pacific Fresh Pool. J Geophys Res Oceans 122(3):1749–1771. https://doi.org/10.1002/2016JC012130

Hackert E, Kovach RM, Molod A, Vernieres G, Borovikov A, Marshak J, Chang Y (2020) Satellite sea surface salinity observations impact on El Niño/Southern Oscillation predictions: case studies from the NASA GEOS seasonal forecast system. J Geophys Res Oceans 125(4):e2019JC015788. https://doi.org/10.1029/2019jc015788

Hajj GA, Zuffada C (2003) Theoretical description of a bistatic system for ocean altimetry using the GPS signal. Radio Sci 38(5):25. https://doi.org/10.1029/2002RS002787

Hasson A, Delcroix T, Boutin J, Dussin R, Ballabrera-Poy J (2014) Analyzing the 2010–2011 La Niña signature in the tropical Pacific sea surface salinity using in situ data, SMOS observations, and a numerical simulation. J Geophys Res Oceans 119(6):3855–3867. https://doi.org/10.1002/2013JC009388

Hasson A, Puy M, Boutin J, Guilyardi E, Morrow R (2018) Northward pathway across the tropical North Pacific Ocean revealed by surface salinity: how do El Niño anomalies reach Hawaii? J Geophys Res Oceans 123(4):2697–2715. https://doi.org/10.1002/2017JC013423

Hasson A, Farrar JT, Boutin J, Bingham F, Lee T (2019) Intraseasonal variability of surface salinity in the eastern tropical pacific associated with mesoscale eddies. J Geophys Res Oceans 124(4):2861–2875. https://doi.org/10.1029/2018JC014175

Hopkins J, Lucas M, Dufau C, Sutton M, Stum J, Lauret O, Channelliere C (2013) Detection and variability of the Congo River plume from satellite derived sea surface temperature, salinity, ocean colour and sea level. Remote Sens Environ 139:365–385. https://doi.org/10.1016/j.rse.2013.08.015

Houndegnonto OJ, Kolodziejczyk N, Maes C, Bourlès B, Da-Allada CY, Reul N (2021) Seasonal variability of freshwater plumes in the eastern Gulf of Guinea as inferred from satellite measurements. J Geophys Res Oceans 126(5):e2020JC017041. https://doi.org/10.1029/2020JC017041

Houtz D, Naderpour R, Schwank M, Steffen K (2019) Snow wetness and density retrieved from L-band satellite radiometer observations over a site in the West Greenland ablation zone. Remote Sens Environ 235:111361. https://doi.org/10.1016/j.rse.2019.111361

Houtz D, Matzler C, Naderpour R, Schwank M, Steffen K (2021) Quantifying surface melt and liquid water on the greenland ice sheet using L-band radiometry. Remote Sens Environ 256:112341. https://doi.org/10.1016/j.rse.2021.112341

Huang P, Lin II, Chou C, Huang R-H (2015) Change in ocean subsurface environment to suppress tropical cyclone intensification under global warming. Nat Commun 6(1):7188. https://doi.org/10.1038/ncomms8188

IOC, SCOR IAPSO (2010) The international thermodynamic equation of seawater—2010: calculation and use of thermodynamic properties, report, Intergovernmental Oceanographic Commission, Manuals and Guides No. 56, UNESCO (English)

Jackson TJ, Schmugge TJ (1991) Vegetation effects on the microwave emission of soils. Remote Sens Environ 36(3):203–212. https://doi.org/10.1016/0034-4257(91)90057-D

Jackson TJ, Gasiewski AJ, Oldak A, Klein M, Njoku EG, Yevgrafov A, Christiani S, Bindlish R (2002) Soil moisture retrieval using the C-band polarimetric scanning radiometer during the Southern Great Plains 1999 Experiment. IEEE Trans Geosci Remote Sens 40(10):2151–2161. https://doi.org/10.1109/TGRS.2002.802480

Jiménez C, Tenerelli J, Prigent C, Kilic L, Lavergne T, Skarpalezos S, Høyer JL, Reul N, Donlon C (2021) Ocean and sea ice retrievals from an end-to-end simulation of the Copernicus Imaging Microwave Radiometer (CIMR) 1.4–36.5 GHz measurements. J Geophys Res Oceans 126(e2021JC017610):7610. https://doi.org/10.1029/2021JC017610

Kaleschke L, Tian-Kunze X, Maaß N, Beitsch A, Wernecke A, Miernecki M, Müller G, Fock BH, Gierisch AMU, Schlünzen KH, Pohlmann T, Dobrynin M, Hendricks S, Asseng J, Gerdes R, Jochmann P, Reimer N, Holfort J, Melsheimer C, Heygster G, Spreen G, Gerland S, King J, Skou N, Søbjærg SS, Haas C, Richter F, Casal T (2016) SMOS sea ice product: operational application and validation in the Barents Sea marginal ice zone. Remote Sens Environ 180:264–273. https://doi.org/10.1016/j.rse.2016.03.009

Kerr YH, Waldteufel P, Wigneron J, Martinuzzi J, Font J, Berger M (2001) Soil moisture retrieval from space: the Soil Moisture and Ocean Salinity (SMOS) mission. IEEE Trans Geosci Remote Sens 39(8):1729–1735. https://doi.org/10.1109/36.942551

Kerr YH, Waldteufel P, Wigneron JP, Delwart S, Cabot F, Boutin J, Escorihuela MJ, Font J, Reul N, Gruhier C, Juglea SE, Drinkwater MR, Hahne A, Martin-Neira M, Mecklenburg S (2010) The SMOS mission: new tool for monitoring key elements of the global water cycle. Proc IEEE 98(5):666–687. https://doi.org/10.1109/jproc.2010.2043032

Kerr YH, Al-Yaari A, Rodriguez-Fernandez N, Parrens M, Molero B, Leroux D, Bircher S, Mahmoodi A, Mialon A, Richaume P, Delwart S, Al Bitar A, Pellarin T, Bindlish R, Jackson TJ, Rudiger C, Waldteufel P, Mecklenburg S, Wigneron JP (2016) Overview of SMOS performance in terms of global soil moisture monitoring after six years in operation. Remote Sens Environ 180:40–63. https://doi.org/10.1016/j.rse.2016.02.042

Kerr YH, Closa J, Zurita A et al (2019a) Cluster analysis report, Cesbio, Toulouse, Report, CESBIO, Toulouse France

Kerr YH Escorihuela MJ et al (2019b) Low frequency passive microwave user requirement consolidation study, report, CESBIO, Toulouse, France

Kerr YH, Rodriguez-Fernandez N, Anterrieu E, Escorihuela MJ, Drusch M, Closa J, Zurita A, Cabot F, Amiot T, Bindlish R, O'Neill P (eds) (2020) The next generation of l band radiometry: user's requirements and technical solutions. In: IEEE international geoscience and remote sensing symposium (IGARSS) electrical network, pp 5974–5977

Kilic L, Prigent C, Aires F, Boutin J, Heygster G, Tonboe RT, Roquet H, Jimenez C, Donlon C (2018) Expected performances of the copernicus imaging microwave radiometer (CIMR) for an all-weather and high spatial resolution estimation of ocean and sea ice parameters. J Geophys Res Oceans 123(10):7564–7580. https://doi.org/10.1029/2018JC014408

Kilic L, Prigent C, Jimenez C, Donlon C (2021) Technical note: a sensitivity analysis from 1 to 40 GHz for observing the Arctic Ocean with the Copernicus Imaging Microwave Radiometer. Ocean Sci 17(2):455–461. https://doi.org/10.5194/os-17-455-2021

Kim H, Lakshmi V (2018) Use of Cyclone Global Navigation Satellite System (CYGNSS) observations for estimation of soil moisture. Geophys Res Lett 45(16):8272–8282. https://doi.org/10.1029/2018GL078923

Kim H, Zohaib M, Cho E, Kerr YH, Choi M (2017a) Development and assessment of the sand dust prediction model by utilizing microwave-based satellite soil moisture and reanalysis datasets in East Asian Desert Areas. Adv Meteorol. https://doi.org/10.1155/2017/1917372

Kim S-B, Van Zyl JJ, Johnson JT, Moghaddam M, Tsang L, Colliander A, Dunbar RS, Jackson TJ, Jaruwatanadilok S, West R (2017b) Surface soil moisture retrieval using the L-band synthetic aperture radar onboard the soil moisture active–passive satellite and evaluation at core validation sites. IEEE Trans Geosci Remote Sens 55(4):1897–1914. https://doi.org/10.1109/TGRS.2016.2631126

Kolodziejczyk N, Hernandez O, Boutin J, Reverdin G (2015) SMOS salinity in the subtropical North Atlantic salinity maximum: 2. Two-dimensional horizontal thermohaline variability. J Geophys Res Oceans 120(2):972–987. https://doi.org/10.1002/2014JC010103

Kolodziejczyk N, Hamon M, Boutin J, Vergely J-L, Reverdin G, Supply A, Reul N (2021) Objective analysis of SMOS and SMAP sea surface salinity to reduce large-scale and time-dependent biases from low to high latitudes. J Atmos Ocean Technol 38(3):405–421. https://doi.org/10.1175/jtech-d-20-0093.1

Laachrate H, Fadil A, Ghafiri A (2019) Soil moisture mapping using SMOS applied to flood monitoring in the Moroccan context. Int Arch Photogramm Remote Sens Spat Inf Sci XLII(4/W12):105–111
Lagerloef GSE, Swift CT, Vine DML (1995) Sea surface salinity: the next remote sensing challenge. Oceanography 8(2):44–50. https://doi.org/10.5670/oceanog.1995.17
Lagerloef G, Colomb FR, LeVine D, Wentz F, Yueh S, Ruf C, Lilly J, Gunn J, Chao Y, deCharon A, Feldman G, Swift C (2008) The Aquarius/SAC-D mission: designed to meet the salinity remote-sensing challenge. Oceanography 21(1):68–81. https://doi.org/10.5670/oceanog.2008.68
Lapointe BE, Brewton RA, Herren LW, Wang M, Hu C, McGillicuddy DJ, Lindell S, Hernandez FJ, Morton PL (2021) Nutrient content and stoichiometry of pelagic Sargassum reflects increasing nitrogen availability in the Atlantic Basin. Nat Commun 12(1):3060. https://doi.org/10.1038/s41467-021-23135-7
Lau WKM, Waliser DE, Hendon H (2012) Air–sea interaction. In: Intraseasonal variability in the atmosphere-ocean climate system. Springer, Berlins
Le Vine DM, Matthaeis PD, Ruf CS, Chen DD (2014) Aquarius RFI detection and mitigation algorithm: assessment and examples. IEEE Trans Geosci Remote Sens 52(8):4574–4584. https://doi.org/10.1109/TGRS.2013.2282595
Leduc-Leballeur M, Picard G, Macelloni G, Mialon A, Kerr YH (2020) Melt in antarctica derived from soil moisture and ocean salinity (SMOS) observations at L band. Cryosphere 14(2):539–548. https://doi.org/10.5194/tc-14-539-2020
Lee T, Lagerloef G, Gierach MM, Kao H-Y, Yueh S, Dohan K (2012) Aquarius reveals salinity structure of tropical instability waves. Geophys Res Lett. https://doi.org/10.1029/2012GL052232
Lee T, Lagerloef G, Kao H-Y, McPhaden MJ, Willis J, Gierach MM (2014) The influence of salinity on tropical Atlantic instability waves. J Geophys Res Oceans 119(12):8375–8394. https://doi.org/10.1002/2014JC010100
Lee T, Fournier S, Gordon AL, Sprintall J (2019) Maritime continent water cycle regulates low-latitude chokepoint of global ocean circulation. Nat Commun 10(1):2103. https://doi.org/10.1038/s41467-019-10109-z
Legeckis R (1977) Long waves in the Eastern equatorial Pacific Ocean: a view from a geostationary satellite. Science 197(4309):1179–1181. https://doi.org/10.1126/science.197.4309.1179
Li Y, Han W, Lee T (2015) Intraseasonal sea surface salinity variability in the equatorial Indo-Pacific Ocean induced by Madden-Julian oscillations. J Geophys Res Oceans 120(3):2233–2258. https://doi.org/10.1002/2014JC010647
Li Y, Yin X, Zhou W, Lin M, Liu H, Li Y (2022) Performance simulation of the payload IMR and MICAP onboard the Chinese ocean salinity satellite. IEEE Trans Geosci Remote Sens 60:1–16. https://doi.org/10.1109/TGRS.2021.3111026
Lievens H, Tomer SK, Al Bitar A, De Lannoy GJM, Drusch M, Dumedah G, Franssen HJH, Kerr YH, Martens B, Pan M, Roundy JK, Vereecken H, Walker JP, Wood EF, Verhoest NEC, Pauwels VRN (2015) SMOS soil moisture assimilation for improved hydrologic simulation in the Murray Darling Basin, Australia. Remote Sens Environ 168:146–162. https://doi.org/10.1016/j.rse.2015.06.025
Liu Z, Kimball JS, Parazoo NC, Ballantyne AP, Wang WJ, Madani N, Pan CG, Watts JD, Reichle RH, Sonnentag O, Marsh P, Hurkuck M, Helbig M, Quinton WL, Zona D, Ueyama M, Kobayashi H, Euskirchen ES (2020) Increased high-latitude photosynthetic carbon gain offset by respiration carbon loss during an anomalous warm winter to spring transition. Glob Change Biol 26(2):682–696. https://doi.org/10.1111/gcb.14863
Madelon R, Rodríguez-Fernández NJ, Schalie RVD, Kerr Y, Albitar A, Scanlon T, Jeu RD, Dorigo W (eds) (2021) Towards the removal of model bias from ESA CCI SM by using an L-band scaling reference. In: 2021 IEEE international geoscience and remote sensing symposium IGARSS, pp 6194–6197
Martin-Neira M (1993) A passive reflectometry and interferometry system (PARIS): application to ocean altimetry. ESA J 17(4):331–355
Martín-Neira M, Oliva R, Corbella I, Torres F, Duffo N, Durán I, Kainulainen J, Closa J, Zurita A, Cabot F, Khazaal A, Anterrieu E, Barbosa J, Lopes G, Tenerelli J, Díez-García R, Fauste J, Martín-Porqueras F, González-Gambau V, Turiel A, Delwart S, Crapolicchio R, Suess M (2016) SMOS instrument performance and calibration after six years in orbit. Remote Sens Environ 180:19–39. https://doi.org/10.1016/j.rse.2016.02.036
McDougall TJ (1987) Thermobaricity, cabbeling, and water-mass conversion. J Geophys Res Oceans 92(C5):5448–5464. https://doi.org/10.1029/JC092iC05p05448
McDougall TJ, Krzysik OA (2015) Spiciness. J Mar Res 73(5):141–152. https://doi.org/10.1357/002224015816665589
McPhaden MJ, Zebiak SE, Glantz MH (2006) ENSO as an integrating concept in earth science. Science 314(5806):1740–1745. https://doi.org/10.1126/science.1132588

McPhaden MJ, Lee T, Fournier S, Balmaseda MA (2020a) ENSO observations. In: El Niño Southern Oscillation in a changing climate

McPhaden MJ, Santoso A, Cai W (2020b) Introduction to El Niño Southern Oscillation in a changing climate. In: El Niño Southern Oscillation in a Changing Climate

Mecklenburg S, Drusch M, Kaleschke L, Rodriguez-Fernandez N, Reul N, Kerr Y, Font J, Martin-Neira M, Oliva R, Daganzo-Eusebio E, Grant JP, Sabia R, Macelloni G, Rautiainen K, Fauste J, de Rosnay P, Munoz-Sabater J, Verhoest N, Lievens H, Delwart S, Crapolicchio R, de la Fuente A, Kornberg M (2016) ESA's Soil Moisture and Ocean Salinity mission: from science to operational applications. Remote Sens Environ 180:3–18. https://doi.org/10.1016/j.rse.2015.12.025

Melnichenko, O, Hacker P, Müller V (2021) Observations of mesoscale eddies in satellite SSS and inferred eddy salt transport remote sensing 13(2): 315. https://doi.org/10.3390/rs13020315

Mohammed PN, Aksoy M, Piepmeier JR, Johnson JT, Bringer A (2016) SMAP L-band microwave radiometer: RFI mitigation prelaunch analysis and first year on-orbit observations. IEEE Trans Geosci Remote Sens 54(10):6035–6047. https://doi.org/10.1109/TGRS.2016.2580459

Molero B, Merlin O, Malbéteau Y, Al Bitar A, Cabot F, Stefan V, Kerr Y, Bacon S, Cosh MH, Bindlish R, Jackson TJ (2016) SMOS disaggregated soil moisture product at 1 km resolution: processor overview and first validation results. Remote Sens Environ 180:361–376. https://doi.org/10.1016/j.rse.2016.02.045

Muñoz-Sabater J, Lawrence H, Albergel C, Rosnay P, Isaksen L, Mecklenburg S, Kerr Y, Drusch M (2019) Assimilation of SMOS brightness temperatures in the ECMWF Integrated Forecasting System. Q J R Meteorol Soc 145(723):2524–2548. https://doi.org/10.1002/qj.3577

Naderpour R, Houtz D, Schwank M (2021) Snow wetness retrieved from close-range L-band radiometry in the western Greenland ablation zone. J Glaciol 67(261):27–38. https://doi.org/10.1017/jog.2020.79

Natali SM, Watts JD, Rogers BM, Potter S, Ludwig SM, Selbmann AK, Sullivan PF, Abbott BW, Arndt KA, Birch L, Björkman MP, Bloom AA, Celis G, Christensen TR, Christiansen CT, Commane R, Cooper EJ, Crill P, Czimczik C, Davydov S, Du J, Egan JE, Elberling B, Euskirchen ES, Friborg T, Genet H, Göckede M, Goodrich JP, Grogan P, Helbig M, Jafarov EE, Jastrow JD, Kalhori AAM, Kim Y, Kimball JS, Kutzbach L, Lara MJ, Larsen KS, Lee BY, Liu Z, Loranty MM, Lund M, Lupascu M, Madani N, Malhotra A, Matamala R, McFarland J, McGuire AD, Michelsen A, Minions C, Oechel WC, Olefeldt D, Parmentier FJW, Pirk N, Poulter B, Quinton W, Rezanezhad F, Risk D, Sachs T, Schaefer K, Schmidt NM, Schuur EAG, Semenchuk PR, Shaver G, Sonnentag O, Starr G, Treat CC, Waldrop MP, Wang Y, Welker J, Wille C, Xu X, Zhang Z, Zhuang Q, Zona D (2019) Large loss of CO2 in winter observed across the northern permafrost region. Nature Climate Change 9(11): 852–857. https://doi.org/10.1038/s41558-019-0592-8

NISAR (2018) NASA-ISRO SAR (NISAR) mission science users' handbook. In: Laboratory, N.J.P. (ed)

Notarnicola C, Angiulli M, Posa F (2008) Soil moisture retrieval from remotely sensed data: Neural network approach versus Bayesian method. IEEE Trans Geosci Remote Sens 46(2):547–557. https://doi.org/10.1109/TGRS.2007.909951

N Ojha (2023) CATDS-CEC-SM L4 DI Monthly global drought indices obtained from SMOS' satellite root zone soil moisture. https://doi.org/10.12770/c85f4b88-bed0-4137-a6c8-6a8b4070bd94

Nyadjro ES, Subrahmanyam B (2016) Spatial and temporal variability of central Indian Ocean salinity fronts observed by SMOS. Remote Sens Environ 180:146–153. https://doi.org/10.1016/j.rse.2016.02.049

Oetting JD, Jen T (2011) The mobile user objective system. Johns Hopkins Apl Tech Digest 30(2):103–112

Ogilvy JA, Merklinger HM (1991) Theory of wave scattering from random rough surfaces. Acoustical Society of America

Olivier L, Boutin J, Reverdin G, Lefèvre N, Landschützer P, Speich S, Karstensen J, Labaste M, Noisel C, RitschelM et al. (2022) Wintertime process study of the North Brazil Current rings reveals the region as a larger sink forCO_2 than expected Biogeosciences 19(12): 2969–2988. https://doi.org/10.5194/bg-19-2969-2022

Olivier L, Reverdin G, Hasson A, Boutin J (2020) Tropical instability waves in the atlantic ocean: investigating the relative role of sea surface salinity and temperature from 2010 to 2018. J Geophys Res Oceans 125(12):e2020JC016641. https://doi.org/10.1029/2020JC016641

Olmedo E, Martínez J, Umbert M, Hoareau N, Portabella M, Ballabrera-Poy J, Turiel A (2016) Improving time and space resolution of SMOS salinity maps using multifractal fusion. Remote Sens Environ 180:246–263. https://doi.org/10.1016/j.rse.2016.02.038

O'Neill P, Bindlish R, Piepmeier J, Le Vine D, Hudson D, Li L, Cruz-Ortiz G, Olney D (eds) (2018) Determination of best low-frequency microwave antenna approach for future high-resolution measuements from space. In: 38th IEEE international geoscience and remote sensing symposium (IGARSS) Valencia, SPAIN, pp 96–99

Paciolla N, Corbari C, Al Bitar A, Kerr Y, Mancini M (2020) Irrigation and precipitation hydrological consistency with SMOS, SMAP, ESA-CCI, Copernicus SSM1km, and AMSR-2 remotely sensed soil moisture products. Remote Sens. https://doi.org/10.3390/rs12223737

Paloscia S, Pettinato S, Santi E, Notarnicola C, Pasolli L, Reppucci A (2013) Soil moisture mapping using Sentinel-1 images: algorithm and preliminary validation. Remote Sens Environ 134:234–248. https://doi.org/10.1016/j.rse.2013.02.027

Parrens M, Al Bitar A, Frappart F, Papa F, Calmant S, Crétaux J-F, Wigneron J-P, Kerr Y (2017) Mapping dynamic water fraction under the tropical rain forests of the Amazonian basin from SMOS brightness temperatures. Water 9(5):350. https://doi.org/10.3390/w9050350

Parrens M, Al Bitar A, Frappart F, Paiva R, Wongchuig S, Papa F, Yamasaki D, Kerr Y (2019) High resolution mapping of inundation area in the Amazon basin from a combination of L-band passive microwave, optical and radar datasets. Int J Appl Earth Observ Geoinform 81(2019):58–71. https://doi.org/10.1016/j.jag.2019.04.011

Pellarin T, Román-Cascón C, Baron C, Bindlish R, Brocca L, Camberlin P, Fernández-Prieto D, Kerr YH, Massari C, Panthou G, Perrimond B, Philippon N, Quantin G (2020) The precipitation Inferred from Soil Moisture (PrISM) near real-time rainfall product: evaluation and comparison. Remote Sens 12(3):481. https://doi.org/10.3390/rs12030481

Picaut J, Hackert E, Busalacchi AJ, Murtugudde R, Lagerloef GSE (2002) Mechanisms of the 1997–1998 El Niño–La Niña, as inferred from space-based observations. J Geophys Res Oceans 107(C5):5-1–5-18. https://doi.org/10.1029/2001JC000850

Piepmeier JR, Johnson JT, Mohammed PN, Bradley D, Ruf C, Aksoy M, Garcia R, Hudson D, Miles L, Wong M (2014) Radio-frequency interference mitigation for the Soil Moisture Active Passive microwave radiometer. IEEE Trans Geosci Remote Sens 52(1):761–775. https://doi.org/10.1109/TGRS.2013.2281266

Piepmeier JR, Focardi P, Horgan KA, Knuble J, Ehsan N, Lucey J, Brambora C, Brown PR, Hoffman PJ, French RT, Mikhaylov RL, Kwack E, Slimko EM, Dawson DE, Hudson D, Peng J, Mohammed PN, Amici GD, Freedman AP, Medeiros J, Sacks F, Estep R, Spencer MW, Chen CW, Wheeler KB, Edelstein WN, O'Neill PE, Njoku EG (2017) SMAP L-band microwave radiometer: instrument design and first year on orbit. IEEE Trans Geosci Remote Sens 55(4):1954–1966. https://doi.org/10.1109/TGRS.2016.2631978

Qu TD, Yu JY (2014) ENSO indices from sea surface salinity observed by Aquarius and Argo. J Oceanogr 70(4):367–375. https://doi.org/10.1007/s10872-014-0238-4

Rahmoune R, Ferrazzoli P, Singh YK, Kerr YH, Richaume PA, Bitar A (2014) SMOS retrieval results over forests: comparisons with independent measurements. IEEE J Sel Top Appl Earth Observ Remote Sens 7(9):3858–3866. https://doi.org/10.1109/jstars.2014.2321027

Rautiainen K, Lemmetyinen J, Schwank M, Kontu A, Menard CB, Matzler C, Drusch M, Wiesmann A, Ikonen J, Pulliainen J (2014) Detection of soil freezing from L-band passive microwave observations. Remote Sens Environ 147(5 May 2014):206–218. https://doi.org/10.1016/j.rse.2014.03.007

Rautiainen K, Parkkinen T, Lemmetyinen J, Schwank M, Wiesmann A, Ikonen J, Derksen C, Davydov S, Davydova A, Boike J, Langer M, Drusch M, Pulliainen J (2016) SMOS prototype algorithm for detecting autumn soil freezing. Remote Sens Environ 180:346–360. https://doi.org/10.1016/j.rse.2016.01.012

Reul N, Saux-Picart S, Chapron B, Vandemark D, Tournadre J, Salisbury J (2009) Demonstration of ocean surface salinity microwave measurements from space using AMSR-E data over the Amazon plume. Geophys Res Lett. https://doi.org/10.1029/2009GL038860

Reul N, Tenerelli J, Boutin J, Chapron B, Paul F, Brion E, Gaillard F, Archer O (2012) Overview of the first SMOS sea surface salinity products. Part I: quality assessment for the second half of 2010. IEEE Trans Geosci Remote Sens 50(5):1636–1647. https://doi.org/10.1109/TGRS.2012.2188408

Reul N, Chapron B, Lee T, Donlon C, Boutin J, Alory G (2014a) Sea surface salinity structure of the meandering Gulf Stream revealed by SMOS sensor. Geophys Res Lett 41(9):3141–3148. https://doi.org/10.1002/2014GL059215

Reul N, Fournier S, Boutin J, Hernandez O, Maes C, Chapron B, Alory G, Quilfen Y, Tenerelli J, Morisset S, Kerr Y, Mecklenburg S, Delwart S (2014b) Sea surface salinity observations from space with the SMOS satellite: a new means to monitor the marine branch of the water cycle. Surv Geophys 35(3):681–722. https://doi.org/10.1007/s10712-013-9244-0

Reul N, Quilfen Y, Chapron B, Fournier S, Kudryavtsev V, Sabia R (2014c) Multisensor observations of the Amazon-Orinoco river plume interactions with hurricanes. J Geophys Res Oceans 119(12):8271–8295. https://doi.org/10.1002/2014JC010107

Reul N, Chapron B, Zabolotskikh E, Donlon C, Quilfen Y, Guimbard S, Piolle JF (2016) A revised L-band radio-brightness sensitivity to extreme winds under Tropical Cyclones: the five year SMOS-storm database. Remote Sens Environ 180:274–291. https://doi.org/10.1016/j.rse.2016.03.011

Reul N, Grodsky SA, Arias M, Boutin J, Catany R, Chapron B, D'Amico F, Dinnat E, Donlon C, Fore A, Fournier S, Guimbard S, Hasson A, Kolodziejczyk N, Lagerloef G, Lee T, Le Vine DM, Lindstrom E, Maes C, Mecklenburg S, Meissner T, Olmedo E, Sabia R, Tenerelli J, Thouvenin-Masson C, Turiel A, Vergely JL, Vinogradova N, Wentz F, Yueh S (2020) Sea surface salinity estimates from spaceborne L-band radiometers: an overview of the first decade of observation (2010–2019). Remote Sens Environ 242:111769. https://doi.org/10.1016/j.rse.2020.111769

Reul N, Chapron B, Grodsky SA, Guimbard S, Kudryavtsev V, Foltz GR, Balaguru K (2021) Satellite observations of the sea surface salinity response to tropical cyclones. Geophys Res Lett 48(1):e2020GL091478. https://doi.org/10.1029/2020GL091478

Reverdin G, Olivier L, Foltz GR, Speich S, Karstensen J, Horstmann J, Zhang D, Laxenaire R, Carton X, Branger H, Carrasco R, Boutin J (2021) Formation and evolution of a freshwater plume in the northwestern tropical Atlantic in February 2020. J Geophys Res Oceans 126(4):25. https://doi.org/10.1029/2020JC016981

Robine J-M, Cheung SLK, Le Roy S, Van Oyen H, Griffiths C, Michel J-P, Herrmann FR (2008) Death toll exceeded 70,000 in Europe during the summer of 2003. CR Biol 331(2):171–178. https://doi.org/10.1016/j.crvi.2007.12.001

Rodríguez-Fernández NJ, Muñoz Sabater J, Richaume P, de Rosnay P, Kerr YH, Albergel C, Drusch M, Mecklenburg S (2017) SMOS near-real-time soil moisture product: processor overview and first validation results. Hydrol Earth Syst Sci 21(10):5201–5216. https://doi.org/10.5194/hess-21-5201-2017

Rodríguez-Fernández NJ, Mialon A, Mermoz S, Bouvet A, Richaume P, Al Bitar A, Al-Yaari A, Brandt M, Kaminski T, Le Toan T, Kerr YH, Wigneron JP (2018) An evaluation of SMOS L-band vegetation optical depth (L-VOD) data sets: high sensitivity of L-VOD to above-ground biomass in Africa. Biogeosciences 15(14):4627–4645. https://doi.org/10.5194/bg-15-4627-2018

Rodríguez-Fernández N, de Rosnay P, Albergel C, Richaume P, Aires F, Prigent C, Kerr Y (2019) SMOS neural network soil moisture data assimilation in a land surface model and atmospheric impact. Remote Sens 11(11):1334. https://doi.org/10.3390/rs11111334

Rodriguez-Fernandez NJ, Anterrieu E, Cabot F, Boutin J, Picard G, Pellarin T, Merlin O, Vialard J, Vivier F, Costeraste J, Palacin B, Rodriguez-Suquet R, Amiot T, Khaazal A, Rouge B, Morel JM, Colom M, Decoopman T, Jeannin N, Caujolle R, Escorihuela MJ, Al Bitar A, Richaume P, Mialon A, Suere C, Kerr YH (eds) (2020). A new L-Band passive radiometer for Earth observation: SMOS-High resolution (SMOS-HR). In: IEEE international geoscience and remote sensing symposium (IGARSS) electrical network, pp 5978–5981

Roman-Cascon C, Pellarin T, Gibon F, Brocca L, Cosme E, Crow W, Fernandez-Prieto D, Kerr YH, Massari C (2017) Correcting satellite-based precipitation products through SMOS soil moisture data assimilation in two land-surface models of different complexity: API and SURFEX. Remote Sens Environ 200:295–310. https://doi.org/10.1016/j.rse.2017.08.022

Ruf CS, Gleason S, Jelenak Z, Katzberg S, Ridley A, Rose R, Scherrer J, Zavorotny V (eds) (2012) The CYGNSS nanosatellite constellation hurricane mission. In: 2012 IEEE international geoscience and remote sensing symposium, pp 214–216

Sadri S, Wood EF, Pan M (2018) Developing a drought-monitoring index for the contiguous US using SMAP. Hydrol Earth Syst Sci 22(12):6611–6626. https://doi.org/10.5194/hess-22-6611-2018

Saji N, Goswami BN, Vinayachandran P, Yamagata T (1999) A dipole mode in the tropical Indian Ocean. Nature 401(6751):360–363. https://doi.org/10.1038/43854

Santi E, Paloscia S, Pettinato S, Fontanelli G (2016) Application of artificial neural networks for the soil moisture retrieval from active and passive microwave spaceborne sensors. Int J Appl Earth Observ Geoinform 48:61–73. https://doi.org/10.1016/j.jag.2015.08.002

Scholze M, Kaminski T, Knorr W, Vossbeck M, Wu M, Ferrazzoli P, Kerr Y, Mialon A, Richaume P, Rodriguez-Fernandez N, Vittucci C, Wigneron JP, Mecklenburg S, Drusch M (2019) Mean European carbon sink over 2010–2015 estimated by simultaneous assimilation of atmospheric CO_2, soil moisture, and vegetation optical depth. Geophys Res Lett 46(23):13796–13803. https://doi.org/10.1029/2019gl085725

Schwank M, Kontu A, Mialon A, Naderpour R, Houtz D, Lemmetyinen J, Rautiainen K, Li QH, Richaume P, Kerr Y, Matzler C (2021) Temperature effects on L-band vegetation optical depth of a boreal forest. Remote Sens Environ 263:112542. https://doi.org/10.1016/j.rse.2021.112542

Shay LK, Goni GJ, Black PG (2000) Effects of a warm oceanic feature on hurricane opal. Mon Weather Rev 128(5):1366–1383. https://doi.org/10.1175/1520-0493(2000)128%3c1366:Eoawof%3e2.0.Co;2

Shoup CG, Subrahmanyam B, Roman-Stork HL (2019) Madden-Julian oscillation-induced sea surface salinity variability as detected in satellite-derived salinity. Geophys Res Lett 46(16):9748–9756. https://doi.org/10.1029/2019GL083694

Song Q, Wang Z (2017) Sea surface salinity observed from the HY-2A satellite, 2017: 8. https://doi.org/10.18063/som.2017.01.004

Stewart KD, Haine TW, Hogg AM, Roquet F (2017) On cabbeling and thermobaricity in the surface mixed layer. J Phys Oceanogr 47(7):1775–1787. https://doi.org/10.1175/JPO-D-17-0025.1

Sun J, Vecchi G, Soden B (2021a) Sea surface salinity response to tropical cyclones based on satellite observations. Remote Sensing 13(3):420. https://doi.org/10.3390/rs13030420

Sun J, Vecchi GA, Soden BJ (2021b) Influence of vertical wind shear on the ocean response to tropical cyclones based on satellite observations. Geophys Res Lett 48(20):e2021GL095451. https://doi.org/10.1029/2021GL095451

Supply A, Boutin J, Reverdin G, Vergely J-L, Bellenger H (2020) Variability of satellite sea surface salinity under rainfall. In: Levizzani V, Kidd C, Kirschbaum DB, Kummerow CD, Nakamura K, Turk FJ (eds) Satellite precipitation measurement, vol 2. Springer, Cham

Supply A, Boutin J, Kolodziejczyk N, Reverdin G, Lique C, Vergely J-L, Perrot X (2022) Meltwater lenses over the Chukchi and the Beaufort seas during summer 2019: From in-situ to synoptic view. J Geophys Res Oceans 127(12):25. https://doi.org/10.1029/2021JC018388

Svoboda R (2000) An introduction to the drought monitor. Drought Netw News 12(1):15–20

Tarasenko A, Supply A, Kusse-Tiuz N, Ivanov V, Makhotin M, Tournadre J, Chapron B, Boutin J, Kolodziejczyk N, Reverdin G (2021) Properties of surface water masses in the Laptev and the East Siberian seas in summer 2018 from in situ and satellite data. Ocean Sci 17(1):221–247. https://doi.org/10.5194/os-17-221-2021

Thomas LN, Shakespeare CJ (2015) A new mechanism for mode water formation involving cabbeling and frontogenetic strain at thermohaline fronts. J Phys Oceanogr 45(9):2444–2456. https://doi.org/10.1175/JPO-D-15-0007.1

Thouvenin-Masson C, Boutin J, Vergely J-L, Reverdin G, Martin ACH, Guimbard S, Reul N, Sabia R, Catany RH, Fanton-d'Andon O (2022) Satellite and in situ sampling mismatches: consequences for the estimation of satellite sea surface salinity uncertainties. Remote Sens 14(8):1878. https://doi.org/10.3390/rs14081878

Tian F, Wigneron J-P, Ciais P, Chave J, Ogée J, Peñuelas J, Ræbild A, Domec J-C, Tong X, Brandt M, Mialon A, Rodriguez-Fernandez N, Tagesson T, Al-Yaari A, Kerr Y, Chen C, Myneni RB, Zhang W, Ardö J, Fensholt R (2018) Coupling of ecosystem-scale plant water storage and leaf phenology observed by satellite. Nat Ecol Evol 2(9):1428–1435. https://doi.org/10.1038/s41559-018-0630-3

Tian-Kunze X, Kaleschke L, Maass N, Makynen M, Serra N, Drusch M, Krumpen T (2014) SMOS-derived thin sea ice thickness: algorithm baseline, product specifications and initial verification. Cryosphere 8(3):997–1018. https://doi.org/10.5194/tc-8-997-2014

Togliatti K, Hartman T, Walker VA, Arkebauer TJ, Suyker AE, VanLoocke A, Hornbuckle BK (2019) (2019) Satellite L-band vegetation optical depth is directly proportional to crop water in the US Corn Belt. Remote Sens Environ 233:111378. https://doi.org/10.1016/j.rse.2019.111378

Tomer SK, Al Bitar A, Sekhar M, Zribi M, Bandyopadhyay S, Kerr Y (2016) MAPSM: a spatio-temporal algorithm for merging soil moisture from active and passive microwave remote sensing. Remote Sens. https://doi.org/10.3390/rs8120990

Trenberth KE, Smith L, Qian T, Dai A, Fasullo J (2007) Estimates of the global water budget and its annual cycle using observational and model data. J Hydrometeorol 8(4):758–769. https://doi.org/10.1175/jhm600.1

Ulaby FT, Batlivala PP, Dobson MC (1978) Microwave backscatter dependence on surface roughness, soil moisture, and soil texture: part I-bare soil. IEEE Trans Geosci Electron 16(4):286–295. https://doi.org/10.1109/TGE.1978.294586

Ulaby FT, Moore RK, Fung AK (1986) Microwave remote sensing: active and passive, vol 3. Artech House, Boston

Verhoest NEC, van den Berg MJ, Martens B, Lievens H, Wood EF, Pan M, Kerr YH, Al Bitar A, Tomer SK, Drusch M, Vernieuwe H, De Baets B, Walker JP, Dumedah G, Pauwels VRN (2015) Copula-based downscaling of coarse-scale soil moisture observations with implicit bias correction. IEEE Trans Geosci Remote Sens 53(6):3507–3521. https://doi.org/10.1109/tgrs.2014.2378913

Vinogradova N, Lee T, Boutin J, Drushka K, Fournier S, Sabia R, Stammer D, Bayler E, Reul N, Gordon A, Melnichenko O, Li L, Hackert E, Martin M, Kolodziejczyk N, Hasson A, Brown S, Misra S, Lindstrom E (2019) Satellite salinity observing system: recent discoveries and the way forward. Front Mar Sci 6:243. https://doi.org/10.3389/fmars.2019.00243

Wagner W, Lindorfer R, Melzer T, Hahn S, Bauer-Marschallinger B, Morrison K, Calvet J-C, Hobbs S, Quast R, Greimeister-Pfeil I, Vreugdenhil M (2022) (2022) Widespread occurrence of anomalous C-band backscatter signals in arid environments caused by subsurface scattering. Remote Sens Environ 276:113025. https://doi.org/10.1016/j.rse.2022.113025

Waldteufel P, Vergely J, Cot C (2004) A modified cardioid model for processing multiangular radiometric observations. IEEE Trans Geosci Remote Sens 42(5):1059–1063. https://doi.org/10.1109/TGRS.2003.821698

Wang H, Magagi R, Goita K, Jagdhuber T (2019) Refining a polarimetric decomposition of multi-angular UAVSAR time series for soil moisture retrieval over low and high vegetated agricultural fields. IEEE J Sel Top Appl Earth Observ Remote Sens 12(5):1431–1450. https://doi.org/10.1109/JSTARS.2019.2909984

Wigneron J-P, Chanzy A, Calvet J-C, Bruguier N (1995) A simple algorithm to retrieve soil moisture and vegetation biomass using passive microwave measurements over crop fields. Remote Sens Environ 51(3):331–341. https://doi.org/10.1016/0034-4257(94)00081-W

Wigneron JP, Waldteufel P, Chanzy A, Calvet JC, Kerr Y (2000) Two-dimensional microwave interferometer retrieval capabilities over land surfaces (SMOS mission). Remote Sens Environ 73(3):270–282. https://doi.org/10.1016/S0034-4257(00)00103-6

Wigneron JP, Jackson TJ, O'Neill P, De Lannoy G, de Rosnay P, Walker JP, Ferrazzoli P, Mironov V, Bircher S, Grant JP, Kurum M, Schwank M, Munoz-Sabater J, Das N, Royer A, Al-Yaari A, Al Bitar A, Fernandez-Moran R, Lawrence H, Mialon A, Parrens M, Richaume P, Delwart S, Kerr Y (2017) Modelling the passive microwave signature from land surfaces: A review of recent results and application to the L-band SMOS & SMAP soil moisture retrieval algorithms. Remote Sens Environ 192(April 2017):238–262. https://doi.org/10.1016/j.rse.2017.01.024

Wu H, Kimball JS, Zhou N, Alfieri L, Luo L, Du J, Huang Z (2019) (2019) Evaluation of real-time global flood modeling with satellite surface inundation observations from SMAP. Remote Sens Environ 233(Novermber 2019):111360. https://doi.org/10.1016/j.rse.2019.111360

Xu X, Shah R, Yueh S, Elder K (eds) (2017) Reflectivity modeling of signals of opportunity for remote sensing of snow and soil moisture. In: 2017 IEEE international geoscience and remote sensing symposium (IGARSS), pp 1438–1440

Yin X, Boutin J, Reverdin G, Lee T, Arnault S, Martin N (2014) SMOS Sea Surface Salinity signals of tropical instability waves. J Geophys Res Oceans 119(11):7811–7826. https://doi.org/10.1002/2014JC009960

Yueh S, Shah R, Xu X, Elder K, Starr B (2020a) Experimental demonstration of soil moisture remote sensing using P-band satellite signals of opportunity. IEEE Geosci Remote Sens Lett 17(2):207–211. https://doi.org/10.1109/LGRS.2019.2918764

Yueh SH, Shah R, Chaubell MJ, Hayashi A, Xu X, Colliander A (2020b) A semiempirical modeling of soil moisture, vegetation, and surface roughness impact on CYGNSS reflectometry data. IEEE Trans Geosci Remote Sens 60:1–17. https://doi.org/10.1109/TGRS.2020.3035989

Yueh SH, Shah R, Xu X, Stiles B, Bosch-Lluis X (2021) A satellite synthetic aperture radar concept using *P*-band signals of opportunity. IEEE J Sel Top Appl Earth Observ Remote Sens 14:2796–2816. https://doi.org/10.1109/JSTARS.2021.3059242

Zavorotny VU, Larson KM, Braun JJ, Small EE, Gutmann ED, Bilich AL (2010) A physical model for GPS multipath caused by land reflections: toward bare soil moisture retrievals. IEEE J Sel Top Appl Earth Observ Remote Sens 3(1):100–110. https://doi.org/10.1109/JSTARS.2009.2033608

Zhu JS, Huang BH, Zhang RH, Hu ZZ, Kumar A, Balmaseda MA, Marx L, Kinter JL (2014) Salinity anomaly as a trigger for ENSO events. Sci Rep 4:6821. https://doi.org/10.1038/srep06821

Zhu J, Kumar A, Wang W (2020) Intraseasonal surface salinity variability and the MJO in a climate model. Geophys Res Lett 47(17):997. https://doi.org/10.1029/2020GL088997

Zribi M, Dechambre M (2003) A new empirical model to retrieve soil moisture and roughness from C-band radar data. Remote Sens Environ 84(1):42–52. https://doi.org/10.1016/S0034-4257(02)00069-X